HYPERCOORDINATE SILICON CNC-PINCER COMPLEXES FOR ELECTRONIC DEVICES

by

Adam Earnhardt

A thesis submitted to the faculty of
The University of North Carolina at Charlotte
in partial fulfillment of the requirements
for the degree of Master of Science in
Chemistry

Charlotte

2022

Approved by:

_____
Dr. Thomas A. Schmedake

_____
Dr. Michael G. Walter

_____
Dr. Yong Zhang

_____
Dr. Daniel Rabinovich

Abstract

ADAM EARNHARDT Hypercoordinate Silicon CNC-Pincer Complexes for Electronic Devices (Under the direction of THOMAS A. SCHMEDAKE)

Previous studies have demonstrated hexacoordinate silicon pincer complexes to be attractive candidates for efficient electron and hole transport layers in organic electronic devices. This work expands the field by incorporating carbon-nitrogen-carbon (CNC) pincer ligands for the first time in hypercoordinate silicon complexes and explores the impact of the ligand on molecular and material properties of the complex. The dianionic 2,6-diphenylpyridine ligand (DPP) was selected for the CNC-pincer studies. 2,6-Di(bromophen-2-yl)pyridine (DPP) was used as a precursor forming the known intermediate dilithiodiphenylpyridine dianion. This dianion was then reacted with either silicon tetrachloride or dichlorodimethylsilane, forming the respective hypercoordinate silicon complex. For comparison, 2,6-bis(benzimidazol-2-yl)pyridine (bzimpy) was also reacted with dichlorodimethylsilane in the presence of triethylamine (TEA) to form the pentacoordinate complex Si(bzimpy)Me_2.

The resulting pentacoordinate complexes were not fully isolated nor implemented into devices due to high reactivity or instability of the Si(pincer)R_2 complexes. The hexacoordinate $Si(DPP)_2$ complex however was quite robust, showing resistance to hydrolysis in NMR solutions of 50:50 DMSO:H_2O and displaying thermally stability to over 420 ℃ and a high T_g (263 ℃). CV data shows an oxidation wave and a reduction wave both of which were partially reversible ($E_{ox,onset}$ = +0.47 V and $E_{red,onset}$ = -2.20 V vs. Fc+1/0), E(HOMO) = -5.27 V and E(LUMO) = -2.60 V and a band gap $\Delta E_{LUMO-HOMO}$ = 2.73 V. Devices were made to test charge mobilities of $Si(DPP)_2$, the three best devices (hole only and electron only) were averaged for their respective

mobilities in the space charge limited current regime resulting in an electron mobility of μe = 1.8×10^{-4} cm^2/Vs and a hole mobility of μh = 1.1×10^{-5} cm^2/Vs.

Acknowledgements

This work would not have been possible without the support and contribution of many of my mentors, colleagues, and friends. Thanks to the National Science Foundation for funding this work, provided by grant #1800331. I'd like to thank my advisor Dr. Tom Schmedake for his unwavering assistance, advice, and guidance. His enthusiasm to explore and ability to stay flexible have shaped my professional growth immensely. I'm extremely grateful for his willingness to dive into any project, whether it be assisting with lab work or setting up a photo shoot for the university. He's an amazing mentor and I'm happy to have had the opportunity to work with him.

I'd like to thank Dr. Michael Walter and Dr. Yong Zhang and all the members of our "silicon supergroup." Though the first meeting was a little intimidating, it put everything into perspective. I greatly appreciate the cross lab and department collaboration that this "supergroup" provided, it really helped to make me see how my projects would fit in to the big picture, develop new ideas and set realistic long term goals.

I'm grateful for Adesola Adeyemi, Micheal Lust, Kate Norman and Askhat Bimukhanov and all the help they've given me in lab these short few years. Though some of our projects weren't feasible, the positivity they brought to lab each day and the eagerness to continue on made those frustrating days only a minor setback. It was truly a wonderful experience working with and mentoring each of you and I'm excited to see what the future holds for you all.

I owe Kevin Boyle many thanks. Not only has he been a huge help in our synthetic and device work, but also in digging through literature, often times finding a new procedure that I'd

missed. Between learning to use Gaussian and cleaning the lab, checking inventory and assiting in reaction set up, Kevin has been an invaluable resource.

I'd also like to thank Margaret Kocherga. Her experience with the synthesis process and device work was extremely helpful in clearing up many hiccups that I had run into during my work. I'm also deeply grateful to her for explaining the wants of industry and how our research goes beyond the lab. Lastly, I'd like to thank Tyler Adams. Not only was he able to quickly develop devices but explain the process in an easy to understand way. Watching the development of the slides into functioning devices was an extremely rewarding and educational opportunity.

TABLE OF CONTENTS

LIST OF TABLES

LIST OF FIGURES

Chapter 1: Hypercoordinate silicon for organic electronics

1.1 Introduction to organic electronics

The history of organic electronics began with the discovery of acceptable electronic properties in organic materials between the 1950's and 1960's. Shortly after, crystals of organic compounds were found to be electroluminescent.[1,2] The field has expanded rapidly since then, to the point where organic electronics offer a host of benefits over traditional electronics. Organic electronics can be printed onto various surfaces, they are often seen as a cheaper alternative, and many of their properties can be tuned with the inclusion of different substituents. In modern times organic electronics are found in a variety of products: signage and displays often use organic light emitting diodes[3], solar cells and detectors in biomedical applications have been made using organic photovoltaics[4,5], and in some cases organic field-effect transistors have been put in electronic paper[6].

One issue that has been endemic with organic electronics is the inablitiy to design and synthesize materials that are fully able to utilize both singlet and triplet excitons[3]. Device architecture is another issue; as the number and type of material components continues to increase. These layers can be exchanged for a variety of reasons, however the most basic devices consist of a metal cathode, an electroluminescence layer (EL), an electron transport layer (ETL) and a hole transport layer (HTL) on an indium tin oxide (ITO) anode[4]. The diagram shown in **Figure 1** uses tris(8-hydroxyquinoline)aluminum(III) (Alq_3) as an EL, N,N′-Di(1-naphthyl)-N,N′- diphenyl-(1,1′-biphenyl)-4,4′-diamine (NPB) as a HTL, and a magnesium/silver alloy as the ETL/cathode. More recent devices have been focused on improving the efficiency and lifetimes of OLED's. Modern devices contain all the components essential for basic devices but with additional materials layered to enhance these qualities. The single emitter device shown on

the left in **Figure 2** is typical for commercial products, each layer shown would have multiple materials[7]. On the right of **Figure 2** is a tandem OLED, which contains multiple emissive layers allowing for a multi-photon emission[8].

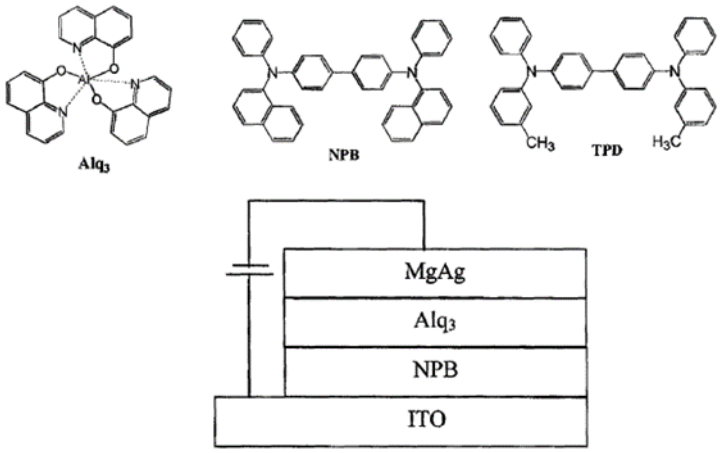

Figure 1: *A basic OLED device and some commonly used component compounds.*[3]

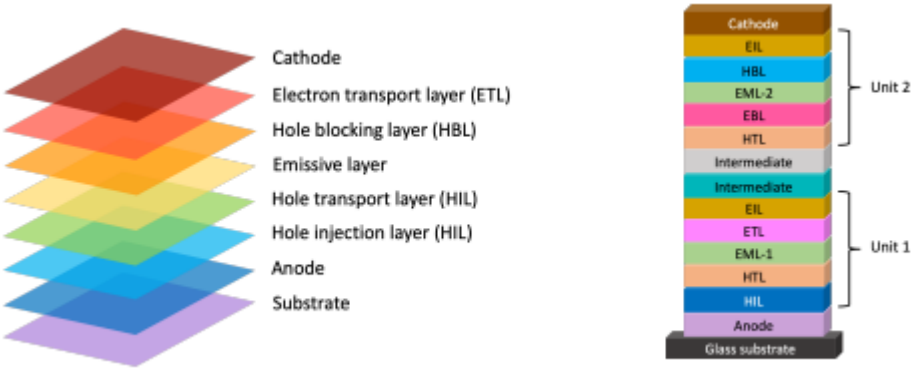

Figure 2: *Modern device structures, image taken from*[9]*. Shown on the left is a single emitter OLED, on the right is a tandem OLED.*

Even with the commercial applications and advancements of OLEDs in recent years, the lighting and electronic industry needs new materials that improve the lifetime, efficiency, and sustainability [10]. Chelated metals have proven to be an invaluable subclass of materials and have been successful in fulfilling the needs of OLED's [11,12]. Synthetically, metal centers offer enhanced tunability for both device properties and molecular properties, as well as regulating

excited state relaxation, limiting molecular rotations, and influencing the range of charge carrier delocalization. An industry paradigm for metal chelates is tris(8-hydroxyquinoline) aluminum (Alq_3). It offers advantageous optoelectronic properties, a high reliability and can be thermally deposited as a high-quality thin film.

Metal chelates have also been adopted to overcome the triplet exciton harvesting problem. When the injected electron and hole recombine in the active region of an OLED, the resulting exciton can be a singlet (formed 25% of the time) or a triplet exciton (75%). Since the excited triplet state (T_1) is inevitably lower energy than the excited singlet state (S_1), and since the relaxation from the T_1 state to the S_0 state is spin-forbidden and prohibitively slow in organic compounds, the triplet excitons are wasted. Ir(III) and Pt(II) complexes have been developed to serve as triplet based phosphors to utilize the triplet excitons and greatly enhance the overall device efficiency[13,14,15].

More recently, thermally activated delayed fluorescence (TADF) has been exploited as an alternative approach to overcoming the triplet exciton harvesting problem[16,17]. This approach avoids the use of rare heavy metals (e.g. Pt and Ir) and instead relies on a synthetically designed small singlet-triplet exciton gap ($\Delta E_{ST} \approx 100$ meV or less) in all-organic compounds. In these materials, thermally induced reverse intersystem crossing converts the non-radiative triplet excitons to emitting singlet excitons. These TADF materials markedly improve the overall lifetime and efficiency, however the rest of the OLED stack layers developed for metal chelate emitters are no longer suitable for the emerging TADF emitters. The need for new electron transport layer materials is particularly urgent, since all of the leading ETLs used by manufacturers are incompatible with the TADF-enabled devices due to stability/purity issues, low triplet exciton energy levels, or low glass transition temperatures (T_g) (**Table 1**). An ideal

ETL for TADF emitters should be chemically stable and easily purified to very high levels of purity (sublimation preferred). To enable full spectrum emitters, the T_1 state should be around 3 eV or greater. The T_g is a particular challenge for many of the existing ETLs. High resistance of the organic layer stack can lead to considerable heating during operation. If the temperature fluctuates around the T_g the resulting phase changes of the ETL lead to strain and dislocation, and device degradation. Despite its otherwise poor performance metrics, the low-cost and high T_g of Alq_3 still make it an attractive ETL for commercial grade devices with triplet phosphors. New ETLs will be needed for the next generation of TADF enabled OLEDs though[18-29].

***Table 1**: Properties of commercial grade ETL materials, problematic properties highlighted in red.*[18-29]

	Stability or purity issues	Retail price ($/g)	e^- mobility ($x10^{-5}cm^2/Vs$)	LUMO (eV)	T_1, triplet exciton (eV)	T_g or MP (°C)
Alq_3	Isomerizes	45	0.4 -1.1	-2.9	2.1	175
T2T	Stable	1034	12	-3.0	2.8	55
BPhen	Stable	108	52	-3.0	2.5	66
TPBi	Stable	566	3.3-8.0	-2.7	2.7	122

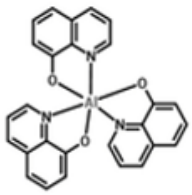

Alq_3

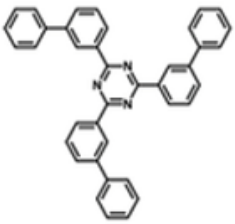

T2T

BPhen

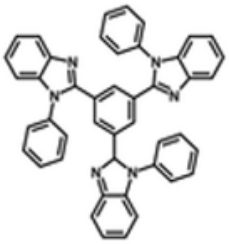

TPBi

1.2 Hypercoordinate silicon

Though most silicon-containing compounds have tetracoordinate, tetravalent silicon atoms, there are numerous examples of stable pentacoordinate and hexacoordinate species.

While some sources use the term hypervalent to describe compounds or complexes in which a main-group atom appears to have exceeded its octet, there is some controversy over the used of this term. Hypercoordinate does not imply a specific type of chemical bonding and side steps this controversy. For this work the term hypercoordinate will be used. One interesting class of pentacoordinate silicon complex are the silatranes studied by Voronkov[30-35]. The pentacoordinate silatranes with their transannular nitrogen-silicon bonds are an important class of compounds that have found use in cross-coupling reactions[36], the immobilization of biomolecules[37], and other pharmacological applications[38]. Another important class of hypercoordinate silicon compounds are silicon porphyrin complexes and other similar macrocycles. Silicon porphyrins and phthalocyanines are hexacoordinate complexes and have been studied in both biological[39] and energy-related fields[40]. With both the silatranes and the silicon porphyrins (**Figure 3)**, the polydentate ligand incorporates the formally neutral nitrogen base site and provides both moisture and thermal stability needed for applications in various other fields.

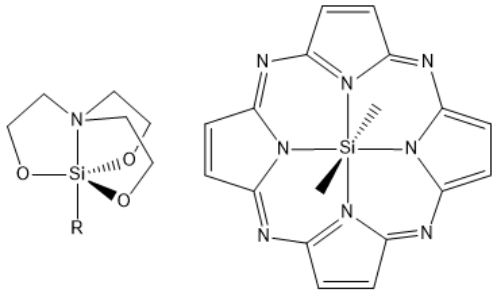

***Figure** 3: Structural examples of both silatranes (left) and the silicon porphyrins (right).*

Non-constrained hemilabile carbon-nitrogen (CN) bidentate ligands or nitrogen-carbon-nitrogen (NCN) tridentate ligands have weak long-range Si-N interactions at most. Thus existing SiC4N2 skeleton framework structural studies are rare. The Cambridge Structural Database has

only one result for this skeleton with a Si-N intramolecular bond of 3 Å or less and no results for 2 Å or less (**Figure 4**).

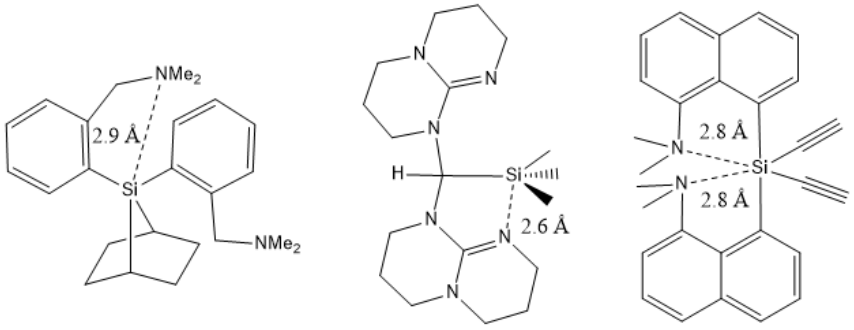

Figure 4: *Structures of hypercoordinate silicon compounds with the framework of SiC4N1 or SiC4N2 reported from the Cambridge Structural Database.*[41-43]

By contrast, the potential for further use of Voronkov's strategy of a polydentate ligand containing a constrained nitrogen-silicon bond is extremely attractive for higher coordinate organosilicon complexes. This suggests that carbon-nitrogen-carbon (CNC) pincer ligands would be attractive for expanding the SiC4N2 framework (**Figure 5**).

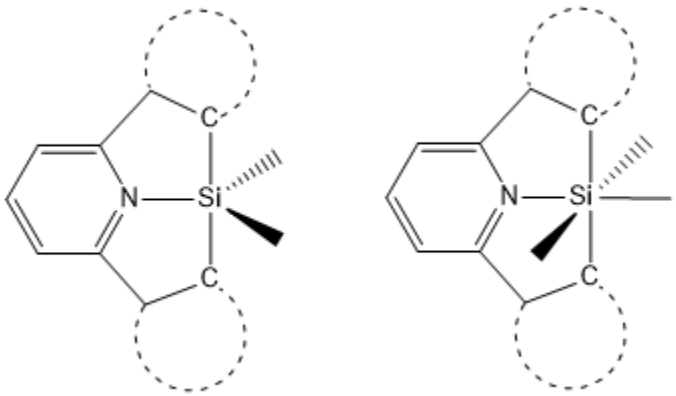

Figure 5: *The general framework of silicon complexes with CNC pincer ligands.*

Further review of the literature shows that in recent years hexacoordinate silicon complexes have found a wide variety of uses. Specifically, a review article written by Peloquin

and Schmedake[44] (**Figure 6**) covered many reported uses of various pyridine-containing ligands in hexacoordinate silicon complexes.

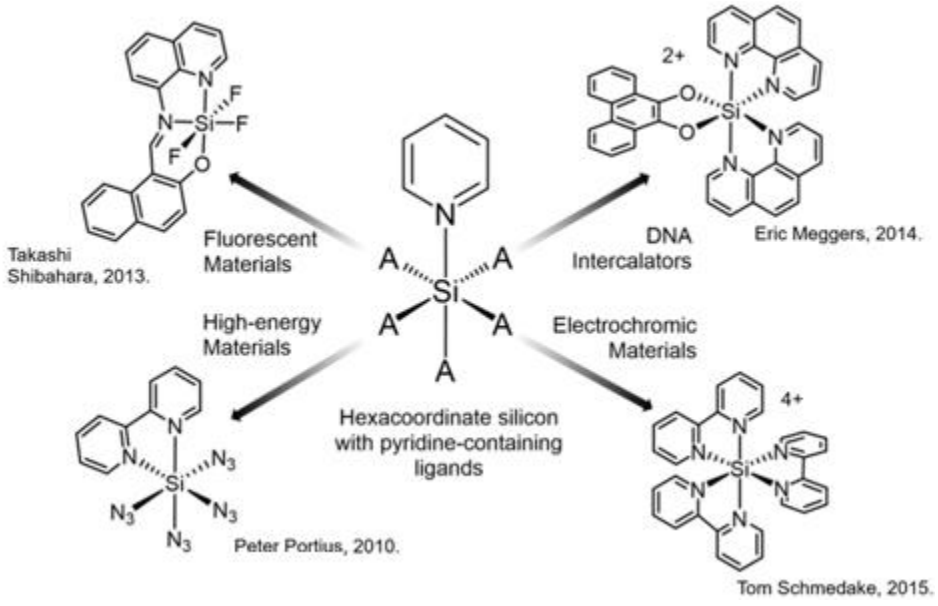

Figure 6: *Some of the various applications of recently reported hexacoordinate silicon complexes containing pyridine are shown above.*

These studies have opened up new avenues of research based on applications that extend past the struture of complexes. The Shibahara[45] paper specifically looked at Shiff base style complexes and their fluorescent properties, providing the opportunity of a new range of photo/electroluminescent materials. Portius[46] studied the potential application of hexacoordinate silicon complexes as high-energy materials. This style of complex could be a very attractive alternative to lead azide, a toxic but widely used explosive. Meggers[47] developed hexacoordinate silicon complexes analogous to some transition metal complexes for biological and pharmaceutical purposes. These were found to be quite stable and resistant to hydrolysis. Lastly, Schmedake[48] showed that the redox chemistry coupled with the stability of the different oxidation states provide possibilities for complexes in electronic applications.

As mentioned by Peloquin and Schmedake, “There is very little information on terpyridine… and other tridentate pyridine-containing ligands that are well known in the transition metal community, which could be excellent ligands for stable hexacoordinate silicon complexes.”[44] The primary focus of the Schmedake research group has since become the study and manufacture of pincer ligand containing hypercoordinate silicon complexes as potential electroactive components in organic electronic devices. Pincer ligands were chosen to investigate ligands common in other areas of coordination chemistry research with Si(pincer)$_2$ motifs (**Figure 7**). There are many additional benefits for using pincer ligands in these complexes: high thermo/chemical stability, tunability of electronic and optical properties, and a uniform deposition of thin films. The pincers chosen for further study include at least one pyridine subunit to assist with stabilization of the complexes.

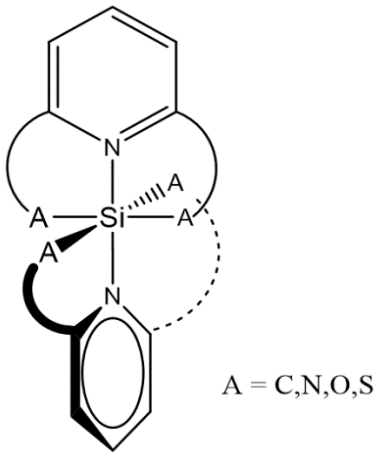

Figure 7: *Shown above is a generalized motif for Si(pincer)$_2$ complexes; carbon and heteroatoms may be used in their formation.*

One of the first complexes investigated was formed using a 2,6-bis(benzimidazol-2-yl)pyridine (bzimpy) pincer ligand. The general reaction scheme for bzimpy and substituted bzimpy compounds can be found in **Figure 8**, the Si(bzimpy)$_2$ complex was found to be air and water stable with potential to be an electron transport or electroluminescent layer. Full

characterization of the complex included thermogravemetric anaylsis (**Figure 9**) and cyclic voltammetry (**Figure 10**) done by Kocherga and colleagues [49].

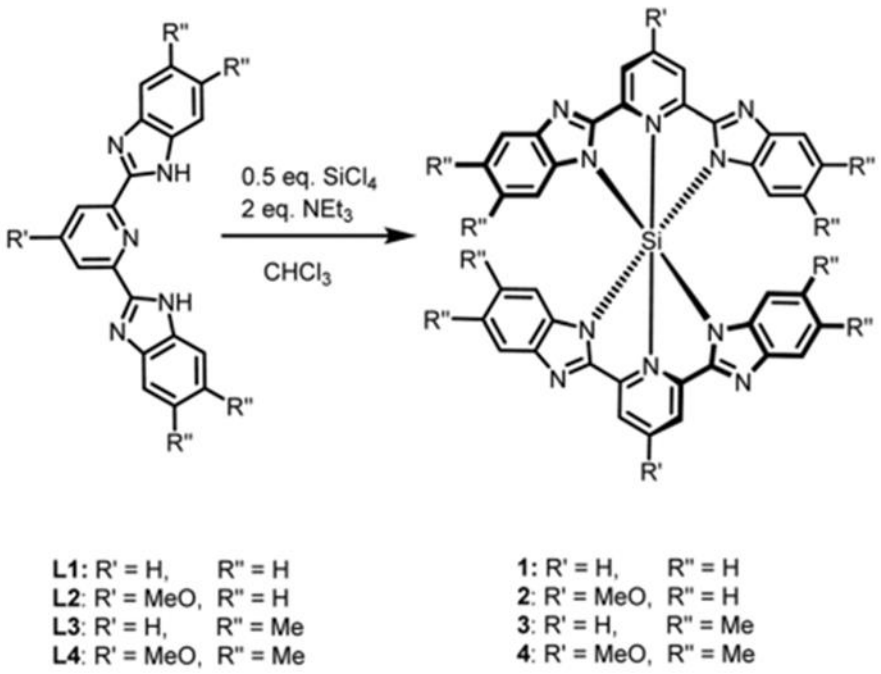

Figure 8: *The general reaction scheme of Si(bzimpy)$_2$ complexes.*[50]

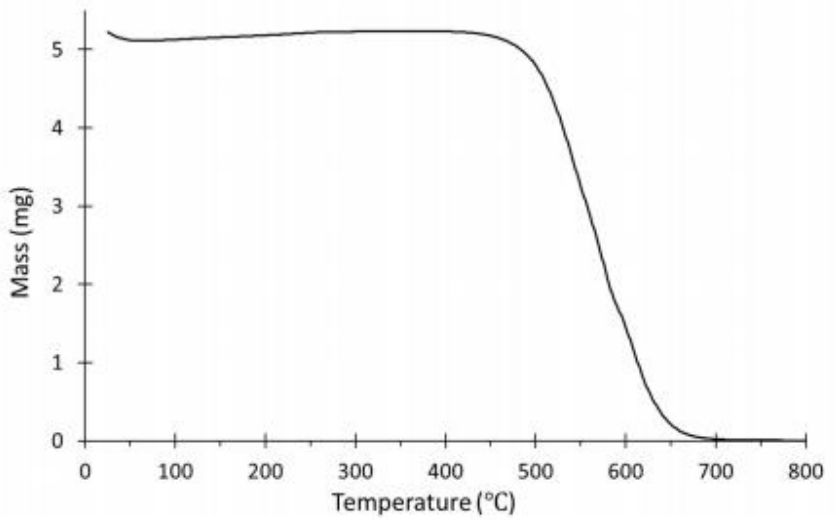

Figure 9: *The TGA data for the Si(bzimpy)$_2$ complex.*

The TGA shows that the complex is quite stable, only beginning to decompose around 500 °C. One issue with the $Si(bzimpy)_2$ complex is the appearant irreversibility of the reduction wave shown in **Figure 10**; this could be due to a multitude of reasons, though the imine position has potential to form a radical, thus hindering reversibility.

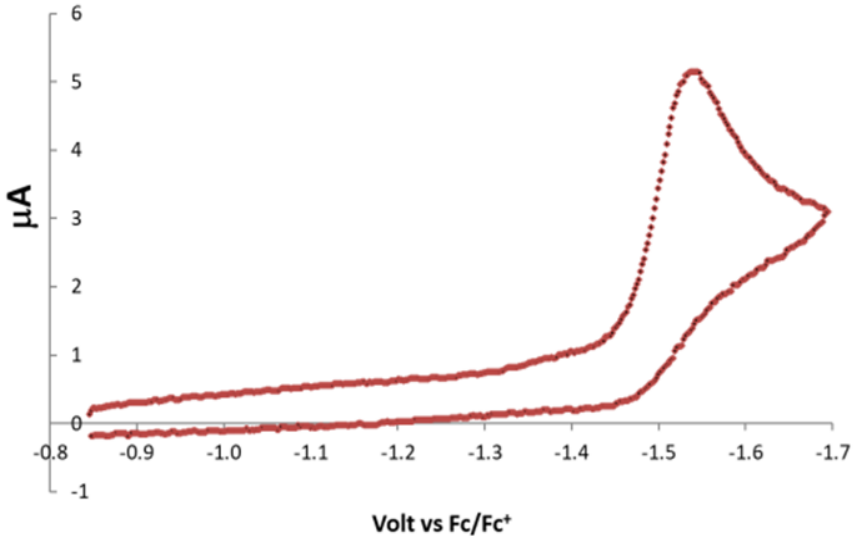

Figure 10: *The cyclic voltammetry ($Si(bzimpy)_2$ in 0.1M $TBAPF_6/CH_3CN$ with a platinum disc working electrode and a scan rate of 200mV/s).*

Despite these potential issues, implementation of the $Si(bzimpy)_2$ complex into devices was successful. Intially, $Si(bzimpy)_2$ was used as an emmisive layer as shown in **Figure 11**, with each subsequent device generation showing higher efficeny.

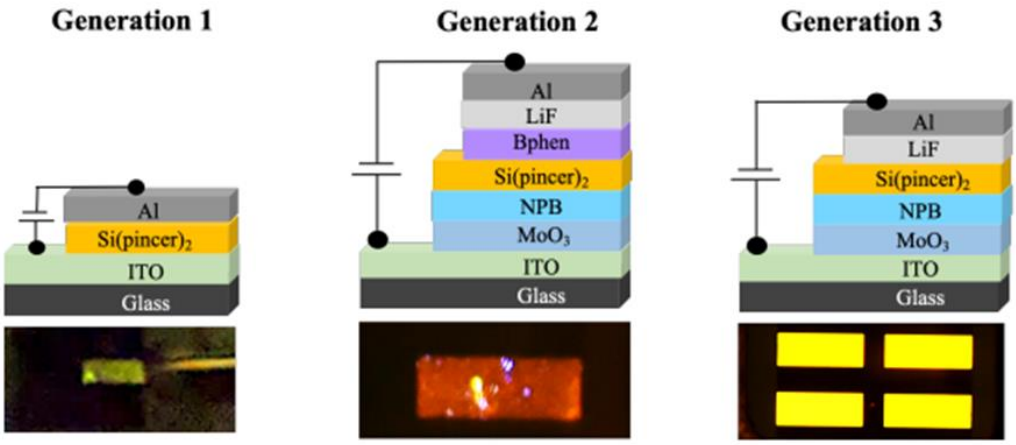

Figure 11: *Generations of device structures with Si(bzimpy)$_2$ as the emissive layer* [9].

The Si(bzimpy)$_2$ motif was further expanded upon recently by targeted functionalization of the ligand as seen in **Figure 8**[50]. The addition of methoxy substituent onto the pyridine (MeObzimpy) or methyl substituents onto the outer most carbons on the benzimidazole (Me$_2$bzimpy) or the combination of the two (MeOMe$_2$bzimpy) allowed for the optoelectronic properties of the complexes to be tuned to some extent. All derivative complexes maintained exceptionally high thermal stabilty, with thermogravimetric analysis showing stability of over 400 °C (**Figure 12).**

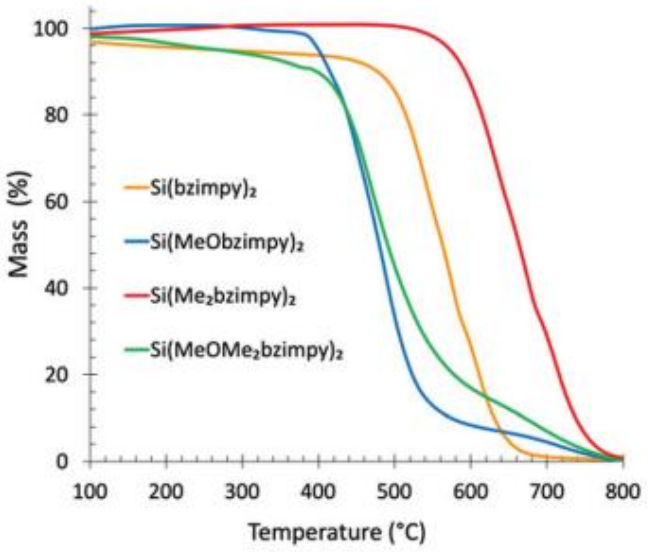

Figure 12: *TGA data for the functionalized bzimpy complexes* [50].

The fluorescence and UV-vis absorption spectra show Si(bzimpy)$_2$ complexes red shifted with the addition of the methyl groups and blue shifted with the addition of the methoxy group (**Figure 13**).

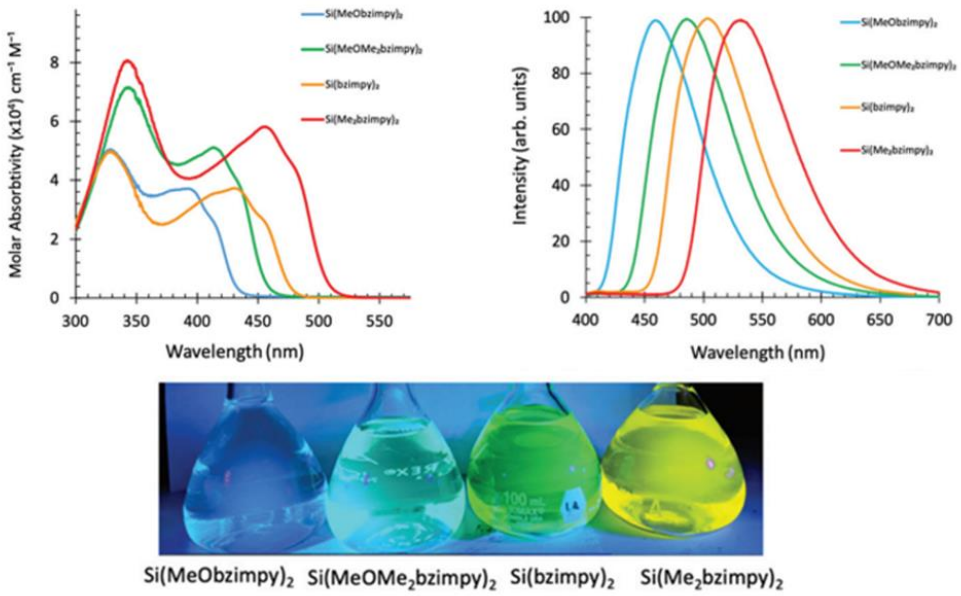

Figure 13: *Optical studies of the bzimpy analogs (uv-vis top left, florescence spectra top right) and appearance in CH_2Cl_2* [50].

Molecular orbital mapping of the complexes show the HOMO is delocalized over the benzimadizole portion of the ligand while the LUMO is spread over the pyridine. With the addition of the electron donating methyl substituents onto the benzimadizole the HOMO energies were raised, thus closing the band gap slightly. Conversly, the methoxy group which was added only on the pyridine moiety raised the energy levels of the LUMO and widened the band gap. The LUMO of all substituted complexes was raised when compared to the base $Si(bzimpy)_2$ complex and the HOMO was raised in all cases except the methoxybzimpy which lowered slightly (**Figure 14**).

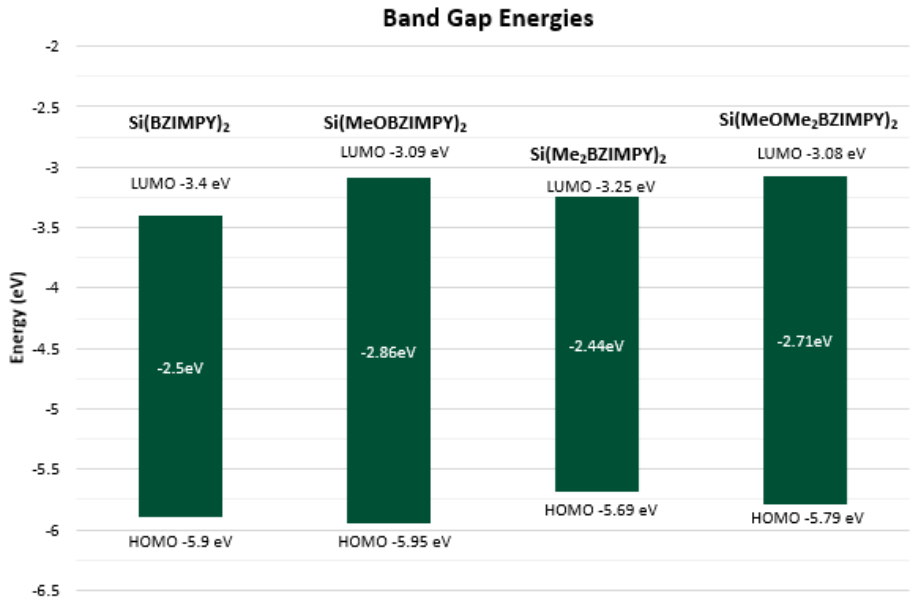

Figure 14: *The comparative band gap energies of bzimpy and bzimpy analog complexes.*

Devices of the complexes were manufactured to measure the charge mobilities. The devices were made by vacuum-deposition on an ITO glass substrate, from there device structures differed: ITO/$Si(bzimpy)_2$/Al for electron mobilities and ITO/PEDOT:PSS/$Si(bzimpy)_2$/Au for hole mobilites. The highest performing devices for electron and hole mobilitiees were made with the base $Si(bzimpy)_2$ complex, however the $Si(Me_2bzimpy)_2$ complex performed only slightly

worse[50] (**Table 2)**. Unfortunately, incorporating the LUMO raising methoxy substituent significantly reduced the charge mobility of the Si(pincer)$_2$ complexes.

Table 2: *Charge mobilities of the Si(bzimpy)$_2$ complexes.*

Complex	**μ_e (cm^2/Vs)**	**μ_h (cm^2/Vs)**
Si(MeObzimpy)$_2$	2.51 X 10^{-8}	1.76 X 10^{-8}
Si(MeOMe$_2$bzimpy)$_2$	4.89 X 10^{-7}	3.19 X 10^{-8}
Si(Me$_2$bzimpy)$_2$	2.94 X 10^{-5}	1.44 X 10^{-6}
Si(bzimpy)$_2$	9.68 X 10^{-5}	5.31 X 10^{-6}

1.3 Contents of this work

This thesis explores the development of hypercoordinate silicon pincer complexes as ETLs for OLED applications, focusing on the CNC-type pincer ligands. The impact of replacing the NNN-bzimpy type pincer motif with a CNC-diphenylpyridine pincer motif is studied to deterimine the impact of the new ligand on the stability and the thermal, material, optical, and electronic properties of the resulting pentacoordinate and hexacoordinate complexes. Prototype devices containing the more stable compounds are also described and charge mobilities of the new transport layer materials are determined. Finally, the leading Si(CNC-pincer)$_2$ complex is compared to existing commercial grade ETL materials and suggestions for additional improvements are proposed.

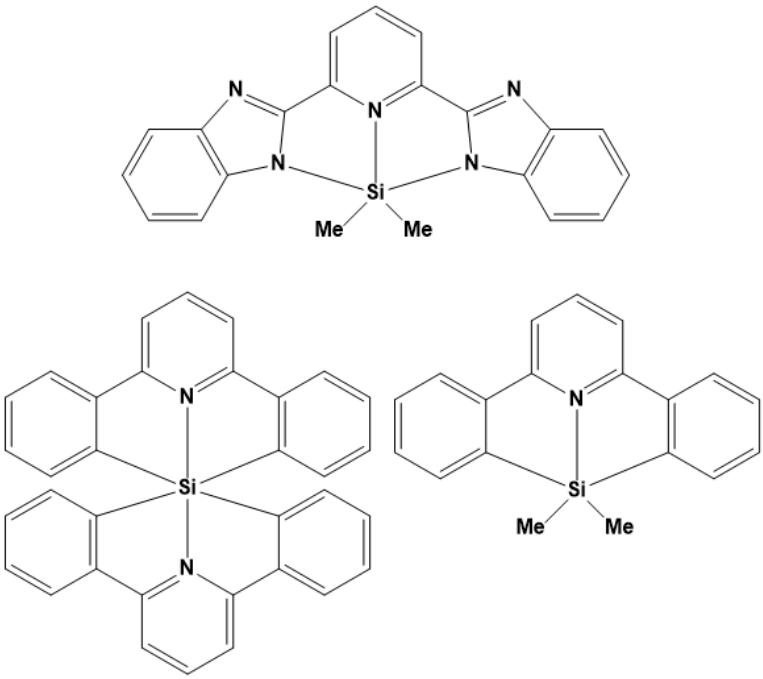

Figure 15: *The complexes synthesized and discussed in this work.*

Chapter 2: Synthesis and characterization of hypercoordinate silicon CNC-pincer complexes

2.1 Ligand selection and synthesis

The diphenylpyridine (DPP) ligand was selected as the CNC-pincer in this study for several reasons. First, the dilithiodiphenylpyridine dianion is a known intermediate formed from the reaction of 2,6-di(bromophen-2-yl)pyridine with $LiBu^n$ and should be a suitable precursor for the formation of pentacoordinate and hexacoordinate silicon pincer complexes (**Figure 16**). Secondly, the diphenylpyridine ligand was predicted to be capable of forming a tridentate, pincer arrangement with a silicon center with only moderate ring strain. Finally, the resulting $Si(DPP)_2$ structure would be reminiscent of the spiro-silabifluorene motif, a motif that has been exploited in a range of hole-transport material due to its high hole mobility and tendency to raise the glass transition temperature due to the perpendicular arrangement of the fluorene substituents[51]. It was anticipated that the $Si(DPP)_2$ structure would also benefit from high charge mobility and that the tortuosity resulting from the two perpendicular diphenylpyridine ligands would produce high T_g.

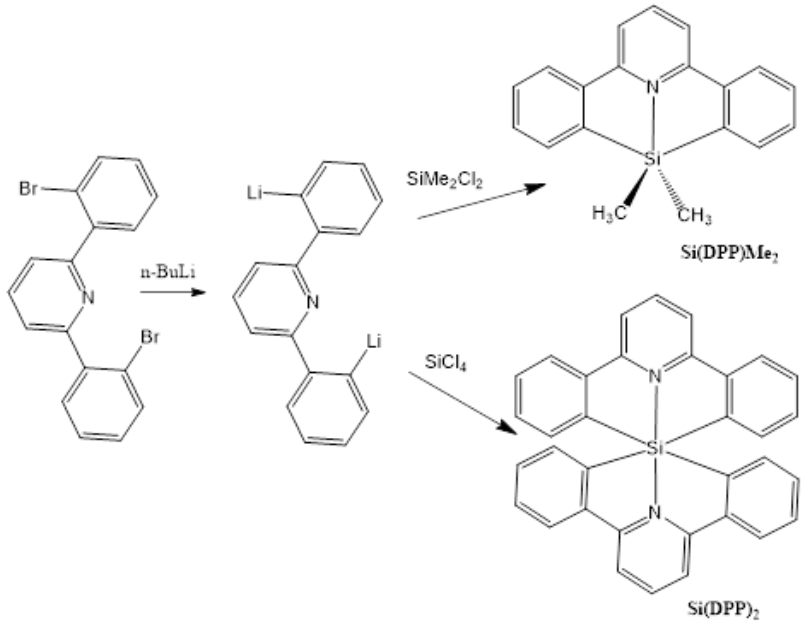

Figure 16: *Proposed synthetic scheme for pentacoordinate and hexacoordinate silicon CNC-pincer complexes.*

The ligand precursor 2,6-di(bromophen-2-yl)pyridine can be synthesized by Suzuki coupling of relatively low-cost reagents 2-bromophenylboronic acid and 2,6-dibromopyridine following the procedure described by Wan and coworkers (**Figure 17**)[52]. The resulting compound was isolated with a typical yield of 43% in our hands, while Wan reports yields of 61%.[52] The relative simplicity and versatility of the Suzuki coupling introduces many options for potential modifications of the $Si(DPP)_2$ platform, but unfortunately lithiation in the subsequent steps limits the synthetic versatility. Benzylic hydrogens, halogens and other groups for example would likely prove problematic with this scheme.

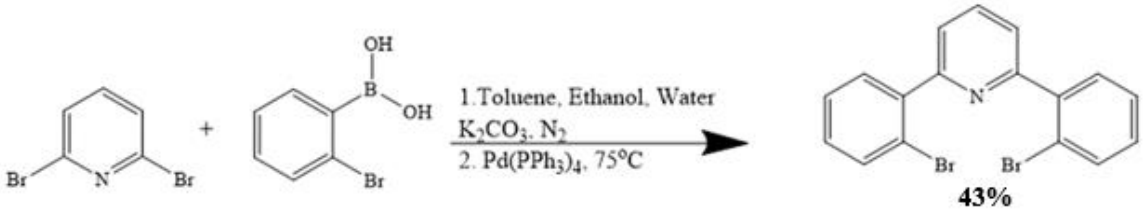

Figure 17: *The synthetic scheme for DBPP.*

2.2 Pentacoordinate complexes[53]

Previous research by Jia and coworkers reported rapid decomposition at ambient temperature for pentacoordinate silicon complexes Si(bip)Ph_2 and Si(bap)Ph_2 (bip = 2,6-bis(2'-indolyl)pyridine and bap = 2,6-bis[2'-(7-azaindolyl)]pyridine)[54]. Since the Si-C bond is less susceptible to hydrolysis than the Si-N bond, we predicted that the reaction of the dilithiodiphenylpyridine dianion with dichlorodialkylsilanes or dichlorodiarylsilanes, SiR_2Cl_2, might provide access to stable, pentacoordinate Si(CNC-pincer)R_2 complexes.

For comparison, the synthesis of the related complex Si(bzimpy)Me_2 was also attempted. The reaction of the bzimpy ligand with excess dichlorodimethylsilane in deuterated chloroform and triethylamine as an HCl scavenger produced the pentacoordinate complex Si(bzimpy)Me_2 (**Figure 18**). ^{29}Si NMR spectroscopy revealed a signal at -74 ppm, consistent with a pentacoordinate silicon complex. MALDI also produced evidence of formation of Si(bzimpy)Me_2 (m/z = 368.8). The resulting complex was extremely susceptible to solvolysis. Since hydrolysis/solvolysis regenerates the bzimpy ligand, a large excess of $SiMe_2Cl_2$ was added to the NMR tube, and crystals of Si(bzimpy)Me_2 were obtained. The NMR tube was shattered under mineral oil, quickly mounted on a nylon loop, and transferred to a 100 K cooled nitrogen stream on the x-ray diffractometer for structure determination.

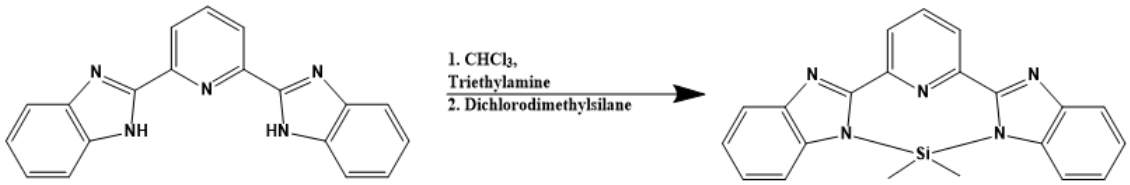

Figure 18: *Reaction scheme for Si(bzimpy)Me2.*

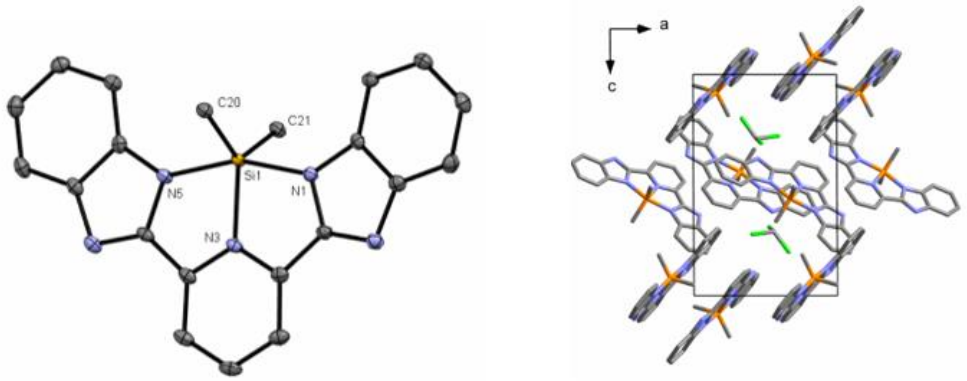

Figure 19: *Crystal structure of Si(bzimpy)Me2*1/2 CHCl3, hydrogen atoms and solvent molecules excluded for clarity. Space group* $P\bar{1}$ *shown as 50% probability ellipsoids.*[52]

The crystal structure of Si(bzimpy)Me2 (**Figure 19**) clearly indicates a pentacoordinate silicon center having a SiC2N3 skeleton, with a planar bzimpy ligand and a distorted trigonal bipyramidal geometry at silicon with the pyridine and methyl substituents occupying the equatorial plane (∠C20-Si-C21= 122.25(7)°, ∠C20-Si-N3= 120.25(6)°, and ∠C21-Si-N3= 117.50(6)°) and the benzimidazole substituents occupying distorted axial positions (∠N5-Si-N1= 159.28°). The short transannular N3-Si bond 1.9085(13)Å is identical to the other two Si-N bonds (1.9065(13)Å and 1.9085(13)Å), a consequence of the steric constraint resulting from the NNN-pincer geometry.[53]

Several attempts to synthetize the pentacoordinate species $Si(DPP)Me_2$ were unsuccessful, although there is evidence of transient formation of this species. The reaction of 2,6-di(bromophen-2-yl)pyridine with 2 equivalents of $LiBu^n$ at -98 ^oC in THF under an argon atmosphere produced the dilithiodianion. This dilithiodianion was subsequently reacted with 1 equivalent of dichlorodimethylsilane (**Figure 20**). The reaction was allowed to stir and slowly warm to room temperature. ^{29}Si NMR indicated a peak at -72 ppm, consistent with the expected signal for a pentacoordinate silicon complex. MALDI of the solution mixture also provided evidence of complex formation with 2 strong peaks corresponding to $[M(-CH_3)]+$, *m/z* = 272.8; [M]+, *m/z* = 288.8.[53] However, all attempts to isolate the product were unsuccessful.

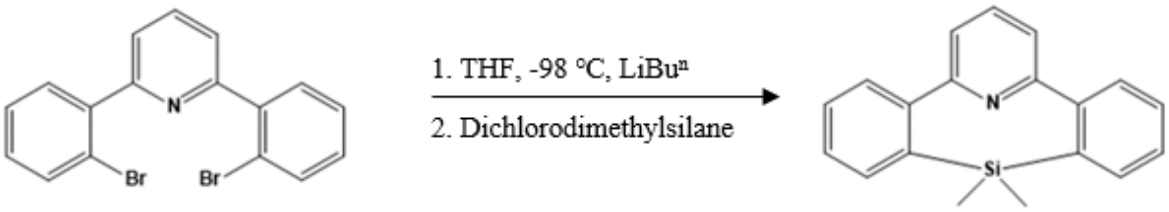

Figure 20: *The reaction scheme for $Si(DPP)Me_2$.*

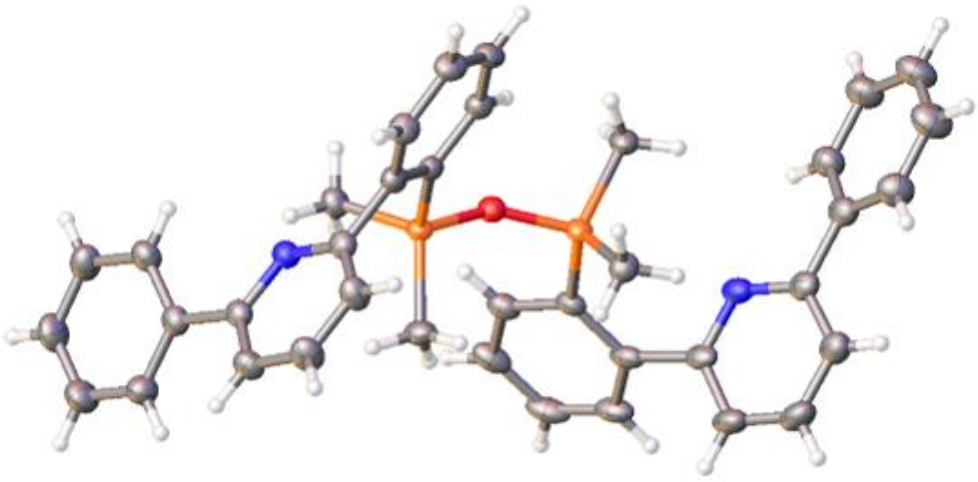

Figure 21: *The hydrolysis product $Si(DPP)Me_2OSi(DPP)Me_2$.*

A similar process to retrieving a crystal sample of Si(bzimpy)Me_2 was followed for Si(DPP)Me_2. Unlike with Si(bzimpy)Me_2, hydrolysis doesn't regenerate a reactive ligand however, and instead crystal of a partial hydrolysis product were obtained from the reaction mixture (**Figure 21**). Interestingly, the C-Si bond (1.89 Å) of the hydrolysis product slightly decreased compared with the C-Si bonds in Si$(DPP)_2$ (1.97 Å, described in section 2.3). The slightly shorter bond length suggests there may be a slight amount of ring strain in the Si-pincer systems that is relieved upon ring opening. Additionally, the hydrolysis product contains a Si-O-Si bridge, with an average Si-O bond length of 1.86 Å somewhat long for a Si-O bond in a disoloxane.

It is uncertain at this time if more stringent water exclusion could lead to isolation of Si(DPP)Me_2. On the one hand, the anticipated greater hydrolysis resistance is evident in the fact that hydrolysis appears to stop following hydrolyis of the first silicon-carbon bond of the Si(DPP)Me_2 complex. Presumably the ring strain and steric crowding around the silicon center is relieved after the first hydrolysis and formation of the disilylether. Nevertheless, the moisture-sensitivity of both pentacoordinate silicon complexes precludes their development as ETL materials in OLED devices, and they were not explored further.

2.3 Hexacoordinate complexes[53]

Reaction of the dilithiodiphenylpyridine dianion with silicon tetrachloride at -98 ^oC in THF produced Si$(DPP)_2$ (**Figure 22**). Isolated yields tended to be poor (around 17%), perhaps due to the ring strain of the 2:1 complex and the possibility of open chain alternatives. Nevertheless, Si$(DPP)_2$ could be isolated as a pale yellow solid. The ^{1}H-NMR spectrum of

$Si(DPP)_2$ indicates one of the aromatic peaks of the DPP ligand shifted to 6.0 ppm due to shielding from the aromatic ring current of the pyridine rings consistent with a kinetically inert hexacoordinate complex in solution. A ^{29}Si-NMR peak at -150 ppm provides further evidence of a hexacoordinate silicon complex in solution. X-ray quality crystals of $Si(DPP)_2$ were obtained from THF (**Figure 23**) and from $CHCl_3$ (**Figure 24**) and used for x-ray structure determination. The hexacoordinate silicon center of $Si(DPP)_2$ adopts a distorted octahedral geometry with nearly planar ligands oriented perpendicular to one another. The Si-N bond is within normal Si-N bonding distances Si1-N1=1.9095(14) Å and Si1-N2 = 1.9126(14) Å. The four Si-C bonds are also within conventional Si-C bond lengths at just under 1.97 Å.[53]

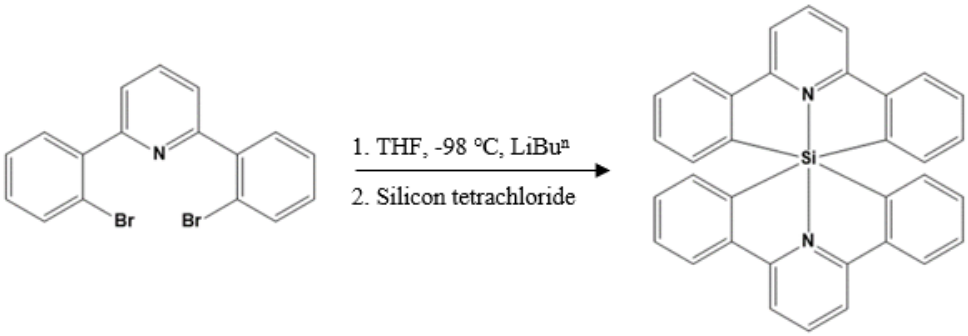

Figure 22: *The reaction scheme for $Si(DPP)_2$.*

Raman spectroscopy was performed on crystals of $Si(DPP)_2$, (Appendix S). The experimental spectrum matched well with predicted Raman spectrum (calculated in gas phase, B3LYP/6–31G*). The band 1043 cm^{-1} in the experimental spectrum matches the 1050 cm^{-1} in the predicted spectrum. This band corresponds to the symmetric stretch (reminiscent of a tetragonal Jahn-Teller distortion) of the SiC4N2 framework and could be a potential identifier for future SiC4N2 complexes. Additionally, the close match of the experimental and calculated spectra provides evidence of the accuracy of the modeling.[53]

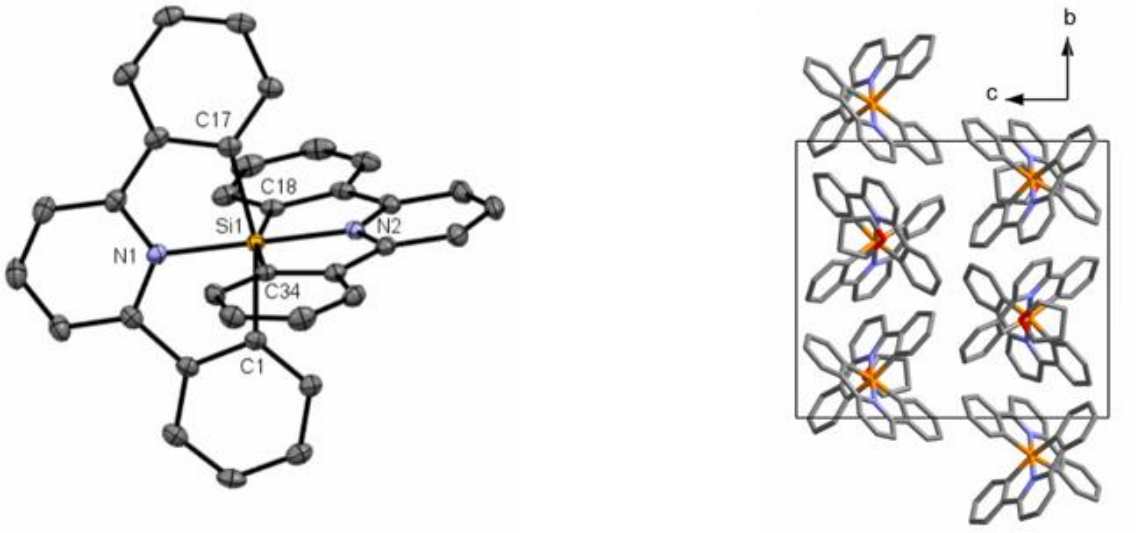

Figure 23: *The crystal structure of Si(DPP)$_2$*THF with space group $P2_1/n$ 50% probability ellipsoids. Hydrogen atoms and solvent molecules excluded for clarity.* [53]

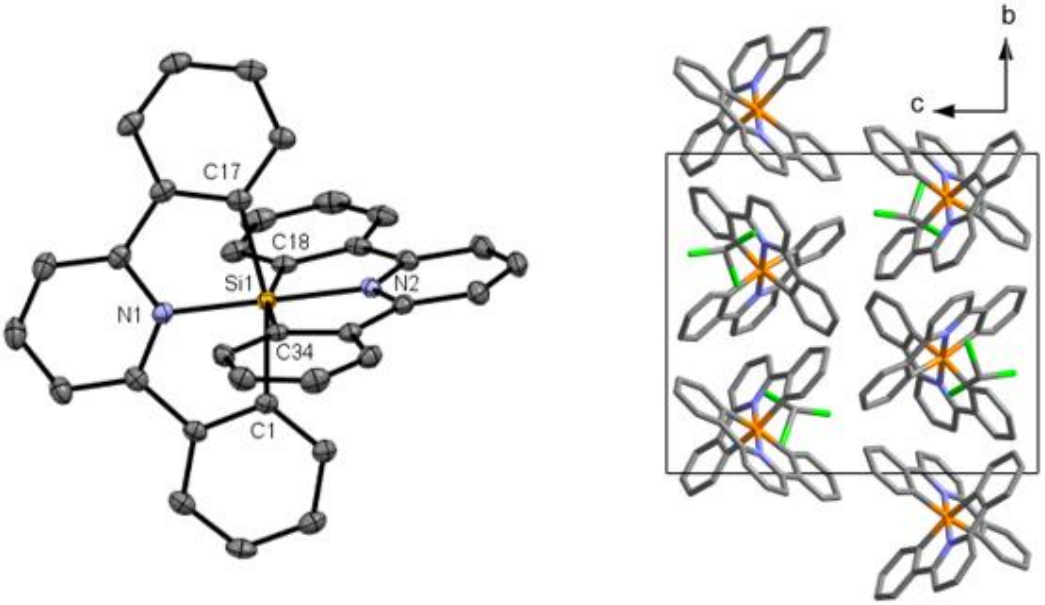

Figure 24: The crystal structure of Si(DPP)$_2$*$CHCl_3$ 50% probability ellipsoids.

Hydrogen atoms and solvent molecules excluded for clarity.[53]The Si(DPP)$_2$ cyclic voltammetry

data (**Figure 25**) shows both an oxidation wave and a reduction wave ($E_{ox,onset}$ = +0.47 V and $E_{red,onset}$ = -2.20 V vs. Fc+1/0, both partially reversible) these values provide a E(HOMO) = -5.27 V and E(LUMO) = -2.60 V and a band gap $\Delta E_{LUMO\text{-}HOMO}$ = 2.73 V. These values were calculated using the equation E(LUMO/HOMO) = -e[$E_{red/ox,onset}$ + 4.8 V]). This is a considerable shift towards higher (less negative) LUMOs and HOMOs compared to Si(bzimpy)$_2$, that has a E(HOMO) = -5.9 V and an E(LUMO) = -3.4 V. This shift was expected from replacing the N-rich bzimpy ligand with the diphenylpyridine ligand. This shift also makes it possible to directly observe both the reduction and oxidation waves for the first time in a Si(pincer)$_2$ complex. In previous studies with Si(bzimpy)$_2$ analogs, only the reduction potential could be observed and only the LUMO directly calculated. The HOMO was then estimated from the optical band gap.[53]

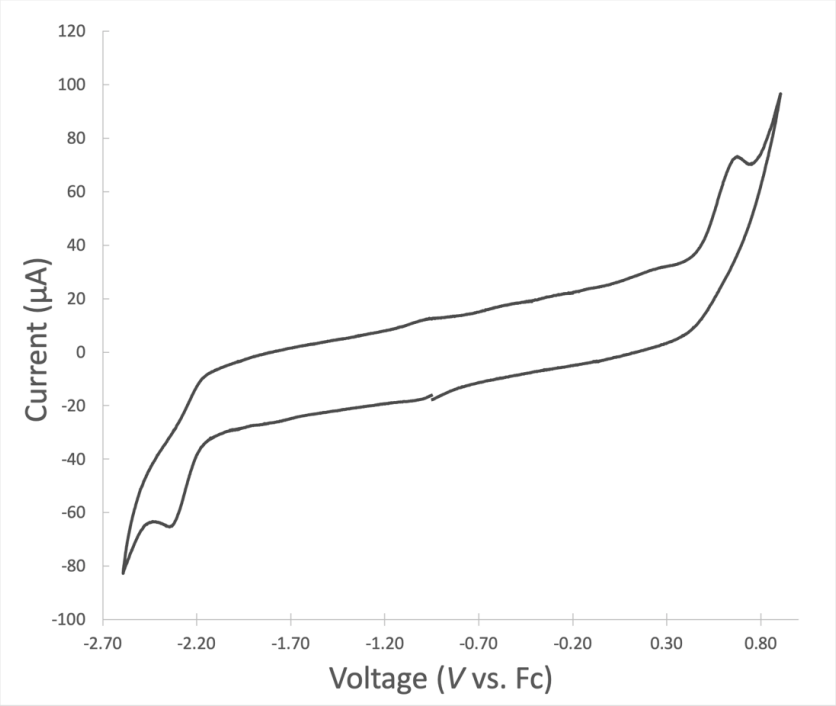

Figure 25: *Cyclic voltammetry data of Si(DPP)$_2$ in DMSO with TBAPF$_6$ and Pt electrode.*[53]

UV-vis spectroscopy of $Si(DPP)_2$ indicates a weak absorbance in the visible spectrum centered at 420 nm, consistent with the pale yellow appearance. To estimate the band gap from the absorbance spectrum, a tangent is drawn to the absorbance curve on the low energy side of the lowest energy peak and extended to the base line. Doing so for $Si(DPP)_2$ indicates an optical band gap of approximately 460 nm or 2.7 eV. Note that this estimate of the band gap is quite close to the band gap determined from cyclic voltammetry, $\Delta E_{LUMO\text{-}HOMO}$ = 2.73 V.[52] This observation provides further validation of using the optical band gap for the estimation of HOMOs for $Si(pincer)_2$ complexes that lack oxidation waves in the solvent window of the cyclic voltammetry experiments (**Figure 26)**.

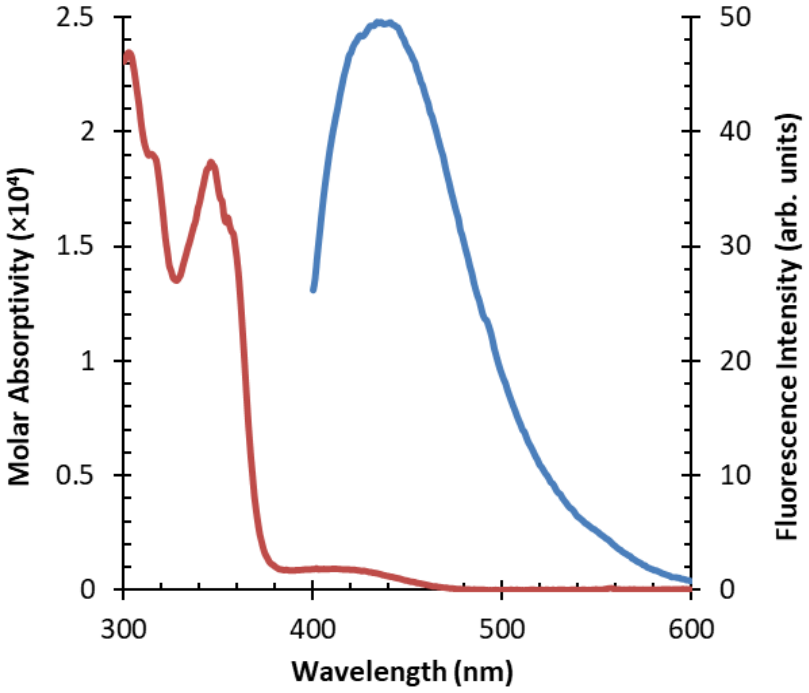

Figure 26: *The UV-Vis (red) spectrum and fluorescence (blue) spectrum of $Si(DPP)_2$ in CH_2Cl_2. Excitation for the fluorescence spectrum was done at 360 nm.*[53]

Despite the low reaction yield, $Si(DPP)_2$ shows remarkable thermal stability. Thermogravimetric analysis was performed at a heating rate of 5 ˚C/min from room temperature to 850 ˚C under ultrapure nitrogen gas. The TGA plot for $Si(DPP)_2$ is shown in **Figure 27**, and the complex appears to be stable up to 420 ℃ at which point roughly half the mass is loss suggesting decomposition through loss of one ligand at a time. DSC was carried out using a heating rate of 5 ^oC /min from room temperature to 400 ^oC under ultrapure nitrogen gas. The DSC curve (Appendix Q) indicates a small endothermic process occurring with an onset at 263 ^oC, which is interpreted as the glass transition temperature (T_g). The complex also appears to be resistant to hydrolysis, no evidence of hydrolysis was observed in the NMR spectra of samples of $Si(DPP)_2$ after 48 hours in a 50:50 mixture of DMSO and water.[53]

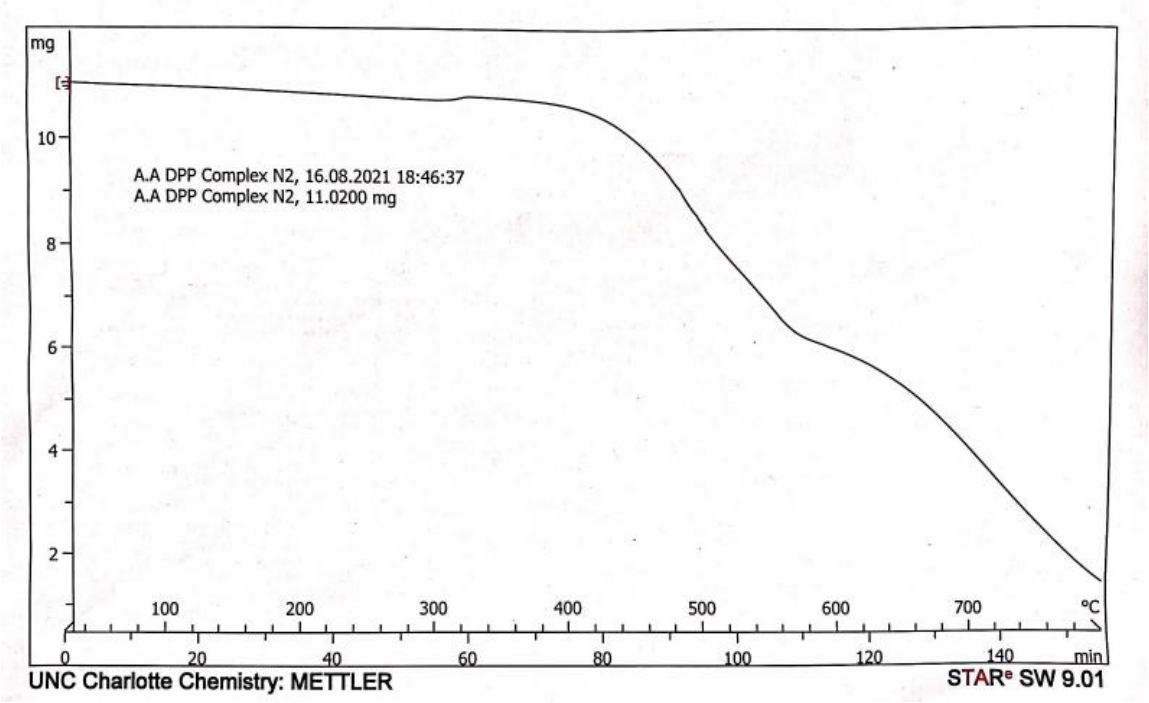

Figure 27: *TGA data recorded for $Si(DPP)_2$*

In conclusion, the DPP ligand does not provide adequate stabilization of pentacoordinate silicon complexes. There is evidence that supports the formation of $Si(bzimpy)Me_2$ and $Si(DPP)Me_2$, but their susceptibility to solvolysis presents a challenge to their utility. Even accidental exposure of $Si(DPP)Me_2$ to air results in partial hydrolysis and ring-opening cleavage of one of the Si-C bonds. On the other hand, sterically protected $Si(DPP)_2$ shows remarkable thermal and chemical stability. Furthermore, the wide bandgap shifted to higher potentials is attractive for OLED applications. The exploration of the material properties and prototype device studies of $Si(DPP)_2$ are explored in Chapter 3.

2.4 Experimental

2.4.1 General[53]

Tetrahydrofuran (THF) was dried using a benzophenone/sodium still and collected fresh before use. 2,6-bis(benzimidazol-2-yl)pyridine and other reagents were purchased and used without additional purification.

All quantum chemical calculations were performed using density functional theory (DFT) [55-58] realized in Gaussian 16 Rev. C.01 program packages. We have performed calculations applying Becke three parameter hybrid functional [59] which uses the non-local correlation provided by the Lee, Yang, and Parr expression [60,61] - B3LYP. As a basis set we have employed standard basis set 6–31G* based on a gaussian type of functions. The combination of functional and basis set was selected based on precision of prediction of the electronic spectrum of silicon hexacoordinated compound $Si(bzimpy)_2$ using time-dependent DFT approach. For all calculated structures optimized structures were obtained. Frequencies calculations demonstrated absence of negative values indicating that all obtained structures correspond to the global minimum. Single-point energy for structures $Si(DPP)_2$ and the symmetric dimer of $Si(DPP)_2$ were −1707.5683 Hartrees and −3415.134410 Hartrees, respectively.

Single crystal X-ray diffraction data of $Si(bzimpy)Me_2 \cdot ½CHCl_3$ was acquired with a Rigaku Gemini Ultra diffractometer using Cu Kα radiation (λ = 1.5418 Å), while diffraction data of $Si(DPP)_2 \cdot THF$ and $Si(DPP)_2 \cdot CHCl_3$ were measured using a Bruker D8 Venture diffractometer with Mo Kα radiation (λ = 0.71073 Å). Suitably sized crystals were coated with a thin layer of oil, mounted on the diffractometer, and flash cooled to 100 K in a nitrogen cold stream. Data were collected using phi and omega scans. CrysAlisPro [62] and Apex3 [63] software

were used to control the diffractometers and perform data reduction. The crystal structures were solved with SHELXS and SHELXT [64]. Alternate cycles of model-building in Olex2 [65] and refinement on F^2 using full-matrix least squares techniques in SHELXL followed. All non-hydrogen atoms were refined anisotropically. All hydrogen atom positions were calculated based on idealized geometries and recalculated after each cycle of least squares. During refinement, hydrogen atom – parent atom vectors were held fixed (riding motion constraint). Crystallographic data is given in **Appendices E, I, P**. Crystallographic data of Si(bzimpy)Me_2·½$CHCl_3$, Si$(DPP)_2$·THF and Si$(DPP)_2$·$CHCl_3$ have been deposited with the Cambridge Structural Database, under deposition numbers 2,109,550–2,109,552.

2.4.2 Synthesis[53]

2,6-bis(2-bromophenyl)pyridine (DBPP): 2,6-dibromopyridine (8.21g, 34.66 mmol), 2-bromo-phenylboronic acid (14.6g, 72.70 mmol), and K_2CO_3 (28.71g, 207.74 mmol) were added to a solvent mixture of toluene (500 mL), ethanol (140 mL), and water (140 mL) in a Schlenk flask. The mixture was stirred and degassed. The flask was then put under a nitrogen environment, using the counterflow of nitrogen gas $Pd(PPh_3)_4$ (2g, 1.73 mmol) was added quickly before resealing the system. The solution was heated to ~75℃ and stirred at this temperature for 24h. The reaction mixture was then cooled to room temperature to provide a yellow suspension that was then put on a rotary evaporator. The resulting solid was then extracted with dichloromethane and water, the organic layer was separated and dried over $MgSO_4$, filtered through Celite, and concentrated down to dryness. The solids were then recrystallized from a DCM/MeOH mixture, washed with MeOH, and dried under vacuum (5.84 g, 43.3% yield). MW= 389.09 g/mole. NMR data is consistent with the reported data from Wan et. al.[52]

Si(bzimpy)Me$_2$: 2,6-bis(benzimidazol-2-yl)pyridine (62 mg, 0.20 mmol) was added to an NMR tube with 1 mL of alumina dried $CDCl_3$. The tube was then sealed with a septum and an excess of triethylamine (100 μL, 0.72 mmol) was added, the tube was then flushed with argon. Dichlorodimethylsilane (100 μL, 0.82 mmol) was then injected. Once finished with the NMR experiments, the NMR tube was set aside and left undisturbed until crystals were formed. The contents of the NMR tube were then poured into a Petri dish containing mineral oil, an appropriate crystal was quickly mounted onto a nylon-loop goniometer head and placed in the cryostream to obtain the x-ray crystal structure. ^{1}H NMR ($CDCl_3$, 500 MHz): δ (ppm relative to TMS) = 0.89 [s, 6H], 7.30 [ddd, 2H, 8.0 Hz, 7.1 Hz, 1.4 Hz], 7.36 [ddd, 2H, 8.0 Hz, 7.7 Hz, 1 Hz], 7.68 [d, 2H, 7.8 Hz], 7.84 [d, 2H, 7.8 Hz], 8.29 [d, 2H, 7.7 Hz], 8.39 ppm [t, 1H]. ^{13}C{^{1}H } NMR ($CDCl_3$, 125 MHz): δ (ppm relative to TMS) = 5.3, 113.9, 118.6, 121.0, 123.1, 124.6, 137.9, 147.2, 148.1, 148.8, 149.6. ^{29}Si NMR ($CDCl_3$, 99 MHz): δ (ppm relative to TMS) = -73.3. MS (MALDI-TOF): MH+, m/z = 368.8 (Appendices A-F).

Attempted synthesis of Si(DPP)Me$_2$: 2,6-bis(2-bromophenyl)pyridine (0.112 g, 0.28 mmol) was placed into a dry Schlenk flask with a stir bar. The flask was degassed before THF (~50 mL) was added. The solution was placed under argon and stirred in a methanol slushy (-98 ℃) for 10 minutes. $LiBu^n$ (0.253 mL, 0.63 mmol) was then added to the flask, and stirred at low temperature for an additional 30 minutes. The solution turned a dark brown/rusty color upon addition. Dichlorodimethylsilane (0.04 mL, 0.32 mmol) was then added to the flask and stirred at -90 ℃ for 1 hour and then gradulally warmed to room temperature. The solution was evaporated under vacuum and put under nitrogen again. CD_2Cl_2 was added to the reaction flask and the resulting solution was used for NMR and MALDI. ^{29}Si NMR (CD_2Cl_2 -d_2, 99 MHz): δ (ppm relative to TMS) = -72. MS (MALDI-TOF): M(-CH3)+, m/z = 272.8; M+, m/z = 288.8

(Appendices G-J). Crystals recovered from old solutions of $Si(DPP)Me_2$ were analyzed by X-ray diffraction. The resulting structure indicated the expected hydrolysis product $(DPP)SiMe_2$-O-$SiMe_2(DPP)$ (**Figure 21**).

$Si(DPP)_2$: 2,6-bis(2-bromophenyl)pyridine (1.22 g, 3.13 mmol) was added into a dry Schlenk flask with a stir bar. Tetrahydrofuran (100 mL) was added to the flask, the system then being degassed and put under a nitrogen atmosphere. The solution was cooled to -98℃ and stirred. The 2.1 equivalents of $LiBu^n$ (2.65 mL, 6.62 mmol) were then added. An aliquot was taken after 10 minutes, the solution being quenched with methanol. The aliquot was then run on GCMS to check for debromination. Upon full debromination, a half equivalent of neat $SiCl_4$ (0.18 mL, 1.56 mmol) was injected and stirred. The reaction solution was kept at -90 ℃ for an additional hour after injection and then left to warm slowly overnight. The solvent was removed the following morning. The resulting crude material was redissolved in 400 mL of boiling THF, filtered and run through a silica gel column (mobile phase: THF). The solution was then evaporated down, resulting in an orange oil. The oil was then treated with diethyl ether and sonicated to form a yellow precipitate. The precipitate was then recrystallized from THF, and washed with chloroform resulting in $Si(DPP)_2$ as a pale yellow solid (130 mg, 17% yield). ^1H NMR (DMSO-d_6, 500 MHz): δ (ppm, relative to TMS) = 6.00 [d, 4H, 7.3 Hz], 6.77 [dd, 4H, 7.3, 7.3 Hz], 6.97 [dd, 4H, 7.3, 7.3 Hz], 8.11 [d, 4H, 7.3 Hz], 8.64, 8.55 [AB2 pattern, 6H, JAB = 7.7 Hz]. $^{13}C\{^1H\}$ NMR (DMSO-d_6, 125 MHz): δ (ppm relative to TMS) = 116.2, 123.7, 124.7, 126.5, 130.1, 134.3 144.0, 152.3, 162.1. ^{29}Si NMR (DMSO-d_6, 99 MHz): δ (ppm relative to TMS) = -150.3. Anal. Calc. for $C_{34}H_{22}N_2Si$: C, 83.92; H, 4.56; N, 5.76. Found: C, 81.87; H, 4.50; N, 5.67%. MS (MALDI-TOF): MH+, m/z = 487.7 (Appendices K-S).

Chapter 3: Device studies

3.1 Device measurements of $Si(DPP)_2$

$Si(DPP)_2$ possesses many of the ideal properties of an effective electron transport layer material, including chemical and thermal inertness, a wide band gap, a high LUMO, and a high T_g. To determine the carrier mobilities of $Si(DPP)_2$, electron-only and hole-only devices were constructed and operated in the space charge limited current regime. The design of the manufactured carrier mobility devices are illustrated in **Figures 28 and 29** with $Si(DPP)_2$ acting as the hole transport and electron transport layer respectively.

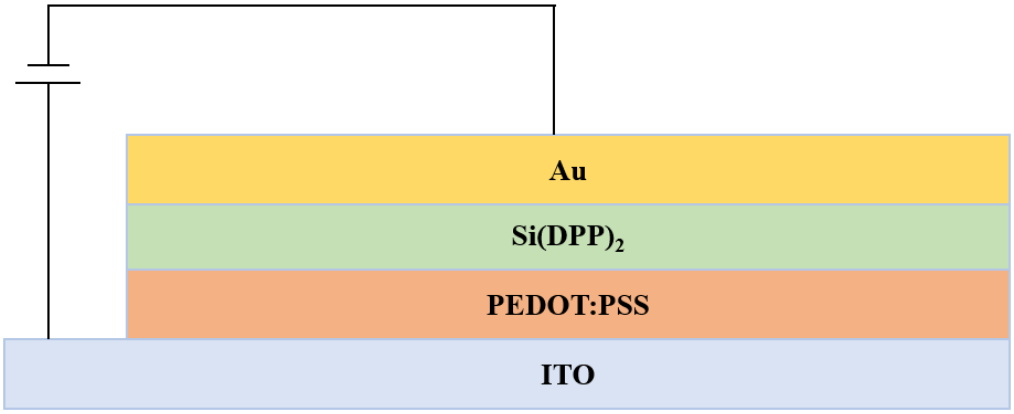

Figure 28: *Device structure used for hole mobility studies.*

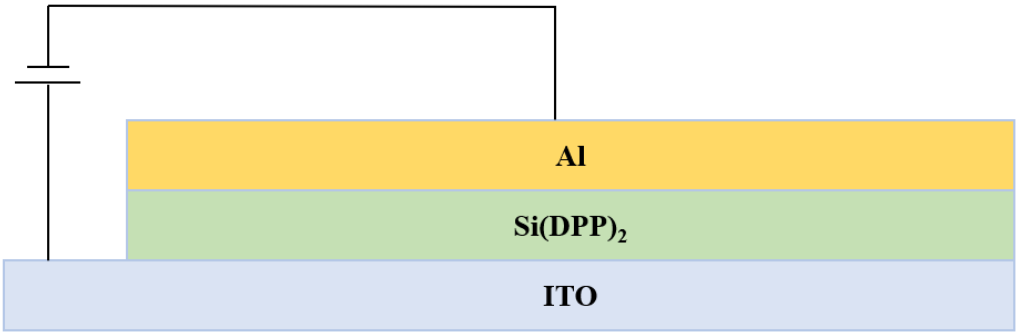

Figure 29: *Device structure used for electron mobility studies.*

Thin films of $Si(DPP)_2$ were successfully deposited on ITO/PEDOT:PSS followed by gold for hole mobility devices and ITO followed by aluminum for electron mobility devices. For hole-only devices $Si(DPP)_2$ was deposited in 173 nm thick films, while the electron-only devices had 100nm thick films. These devices were manufactured in a glove box containing a thermal evaporation system. **Figure 30** shows the Log(J)-log(V) plots made to confirm that the devices were operating in a space-charge limited current regime. The best three curves from both sets of devices, electron only and hole only, were averaged for the their respected mobilities to obtain an electron mobility of $\mu_e = 1.8\times10^{-4}$ $cm^2V^{-1}s^{-1}$ and a hole mobility of $\mu_h = 1.1\times10^{-5}$ $cm^2V^{-1}s^{-1}$ with standard deviations of 0.92×10^{-5} $cm^2V^{-1}s^{-1}$ and 11×10^{-5} $cm^2V^{-1}s^{-1}$ respectively.[53]

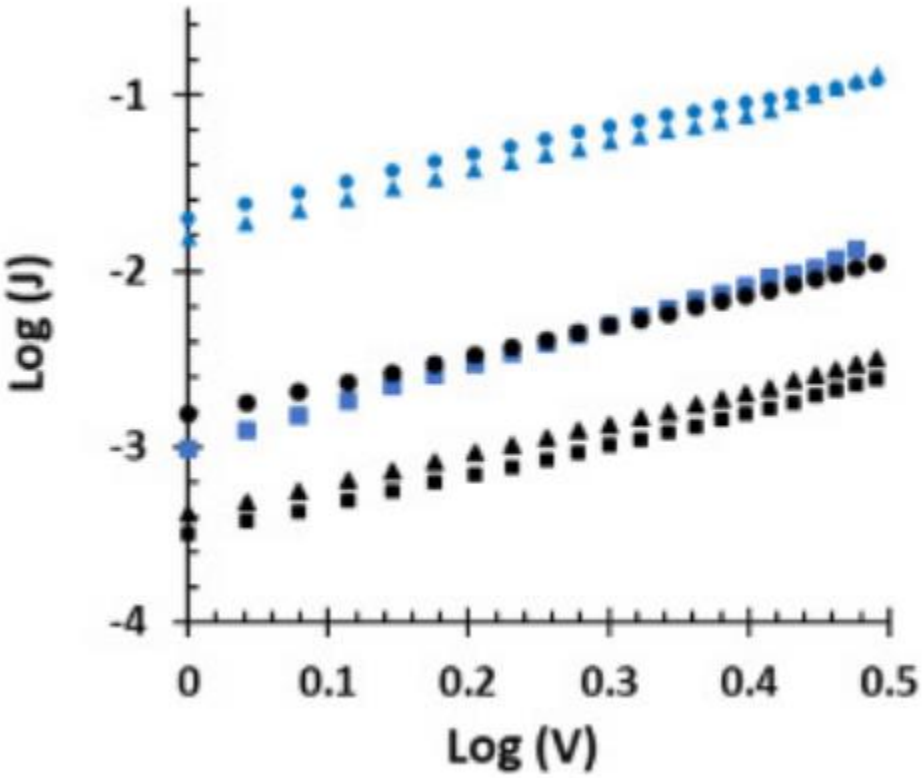

Figure 30: *The Log(J)-log(V) charge mobility curves for hole mobility devices (black) and electron mobility devices (blue). The surface area for all films was 6.0x10^{-6}m^{2}.*[53]

Computataional modeling was utilized to probe the electronic properties and bipolar charge transport of Si(DPP)$_2$. The geomtry of Si(DPP)$_2$ was optimized with density functional theory (DFT) using the functional B3LYP and the basis set 6-31G* in Gaussian 16. The resulting optimized geometry was consistent with the observed crystal structure. The calculated LUMO of Si(DPP)$_2$ is a delocalized pi-orbital spread out over the entire molecule as is tyipcal of other Si(pincer)$_2$ complexes. Unlike the Si(bzimpy)$_2$ analogs however, the HOMO of Si(DPP)$_2$ has a delocalized σ-orbital symmetry around the SiC_4 plane (**Figure 31**). The orthogonality of the LUMO and HOMO may account for the weak transitions observed for the $S_0 \rightarrow S_1$ and $S_0 \leftarrow S_1$ transitions in the UV-Vis and fluorescence spectra.[53]

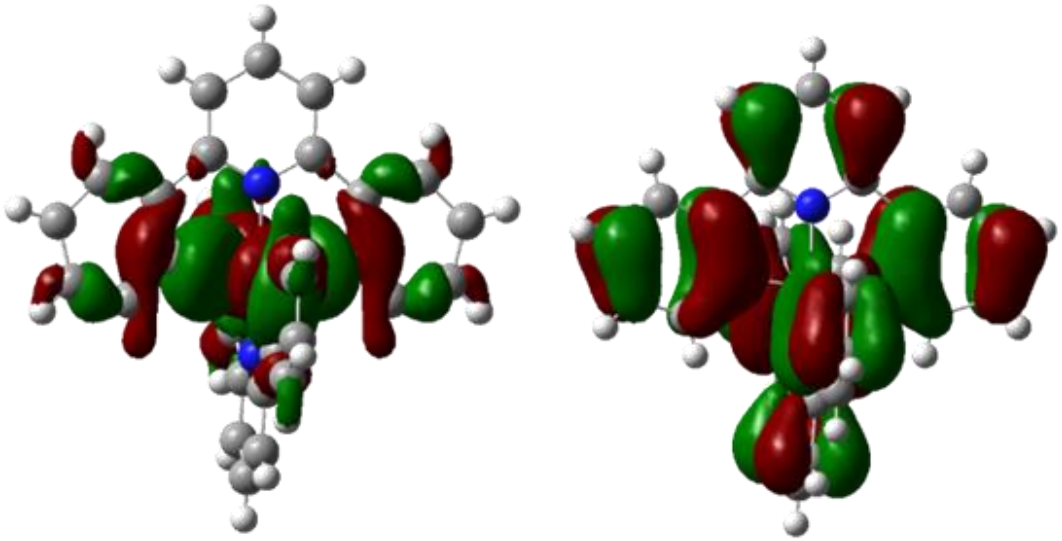

Figure 31: *HOMO (left) and LUMO (right) of Si(DPP)$_2$.*

The σ-based HOMO may also explain why the hole mobility is about an order of magnitude lower than the electron mobility. To clarify this issue, charge mobilities of Si(DPP)$_2$ were estimated using Marcus-Hush theory for the symmetric case where $\Delta G^o = 0$.[66,67] equation 1. In this equation, $\lambda_{electron/hole}$ refers to the reorganization energy of the electron or hole respectively. The reorganization energy is the energy required to convert the nuclear coordinates of the reactants to the nuclear coordinates of the products without actually transferring an electron. Generally speaking, the more delocalized the electron or hole, the lower the reorganization energy is and the faster the rate of electron transfer becomes. Single point energy calculations were used to determine $\lambda_{electron/hole}$ from equations 2 and 3, where $E^+(A)$ would correspond to a single point energy calculation of a +1 charged species (E^+) with the optimized geometry of the neutral molecule (A). Likewise, $E(A^-)$ would be the single point energy of a neutral molecule with the optimized geometry of the anionic species (A^-).[53]

$$K_{h/e} = \left(\frac{\pi}{\lambda_{h/e} k_B T}\right)^{1/2} \times \frac{V_{h/e}^2}{\hbar} \times exp\left(\frac{-\lambda_{h/e}}{4 k_B T}\right) \quad \text{eq. 1}$$

$$\lambda_{hole} = [E^+(A)+E(A^+)]-[E^+(A^+)+E(A)] \quad \text{eq. 2}$$

$$\lambda_{electron} = [E^-(A)+E(A^-)]-[E^-(A^-)+E(A)] \quad \text{eq. 3}$$

$$V_{h/e} = \frac{E_{HOMO/LUMO+1} - E_{HOMO-1/LUMO}}{2} \quad \text{eq. 4}$$

$$D = 0.5kr^2 \quad \text{eq. 5}$$

$$\mu = eD/k_B T \quad \text{eq. 6}$$

The electronic coupling (tunneling matrix) $V_{h/e}$ was determined using the method of energy splitting in dimer and Koopman's theorem (KT-ESD method). In this method, a dimer of the molecule of interest is optimized and half the difference of the splitting of the HOMO (or LUMO) is used as the value of V_h (or V_e) as shown in equation 4. To eliminate differences in site energies, it is better to use a symmetrical dimer (related by an inversion center) (**Figure 32**). Once $V_{h/e}$ and $\lambda_{electron/hole}$ were calculated, the rates for electron transfer were calculated using equation 1. The rate was then converted to a diffusion constant using equation 5 and converted to a mobility using equation 6. The results of all calculations are shown in Table 3 along with the experimentally determined mobilities.[53]

The resulting calculated mobilities match up reasonably well with the experimentally determined mobility values (**Table 3)**. Both calculated results are within an order of magnitude of the experimental results. As expected, despite the reasonably low hole reorganization energy, the poor intermolecular overlap of the σ-based HOMO results in a very low electronic coupling term V_h. Consequently, the overall calculated hole mobility is significantly lowered. The low

hole mobility is not a significant concern for ETL materials, but for other applications where a higher hole mobility is desired σ-based HOMOs should probably be avoided.

On the other hand, the electron mobility $\mu_e = 1.8\times10^{-4}$ $cm^2V^{-1}s^{-1}$ (std. dev. 1.1×10^{-4} $cm^2V^{-1}s^{-1}$) is the highest electron mobility ever measured for a $Si(pincer)_2$ complex. Modeling suggests the high mobility can be attributed to both a moderately low reorganization energy and a moderately high electronic coupling term. The close match between theory and experiment also suggests computational modeling could be used to identify additional target compounds for synthetic efforts in the future.[53]

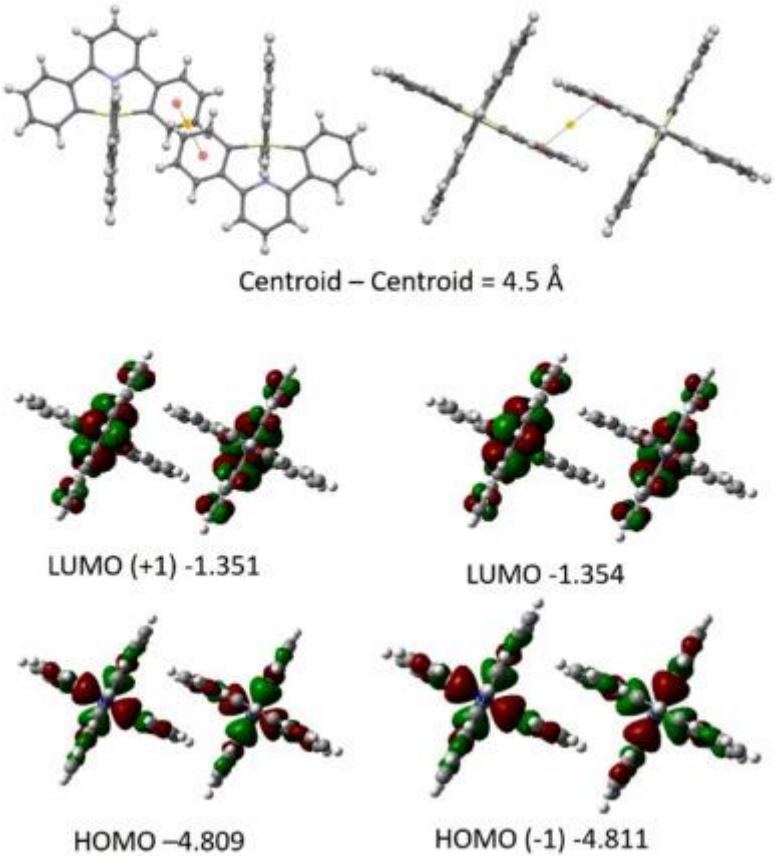

Figure 32: *Symmetrical dimer (top) and resulting frontier orbitals (bottom) used for electronic coupling constant determination.*[53]

Table 3: *Calculated and experimental charge mobility data*

	h^+	e^-
$\lambda_{calc(h/e)}$	248 meV	345 meV
$V_{calc(h/e)}$	0.14 meV	2.0 meV
$\mu_{calc(h/e)}$	3.5×10^{-5} $cm^2V^{-1}s^{-1}$	8.8×10^{-5} $cm^2V^{-1}s^{-1}$
$\mu_{exp(h/e)}$ **st.dev.**	1.1×10^{-5} (9.2×10^{-6}) $cm^2V^{-1}s^{-1}$	1.8×10^{-4} (11×10^{-5}) $cm^2V^{-1}s^{-1}$

3.2 Comparisons with other Si(pincer)$_2$ and ETLs

Si(DPP)$_2$ represents a step in the right direction for developing Si(pincer)$_2$ complexes for ETL applications. A comparative band edge diagram was constructed using the experimentally determined HOMO/LUMO values from cyclic voltammetry of Si(DPP)$_2$ and Si(bzimpy)$_2$ (**Figure 33**). The DPP complex has both a higher HOMO and LUMO and a wider band gap than most bzimpy analogs. An ideal ETL for TADF devices would have a LUMO around -2.0 eV and

band gap of 4.0 eV. Clearly $Si(DPP)_2$ does not hit these values yet, but the DPP ligand appears to be a significant improvement over the NNN-pincer ligands explored previously.

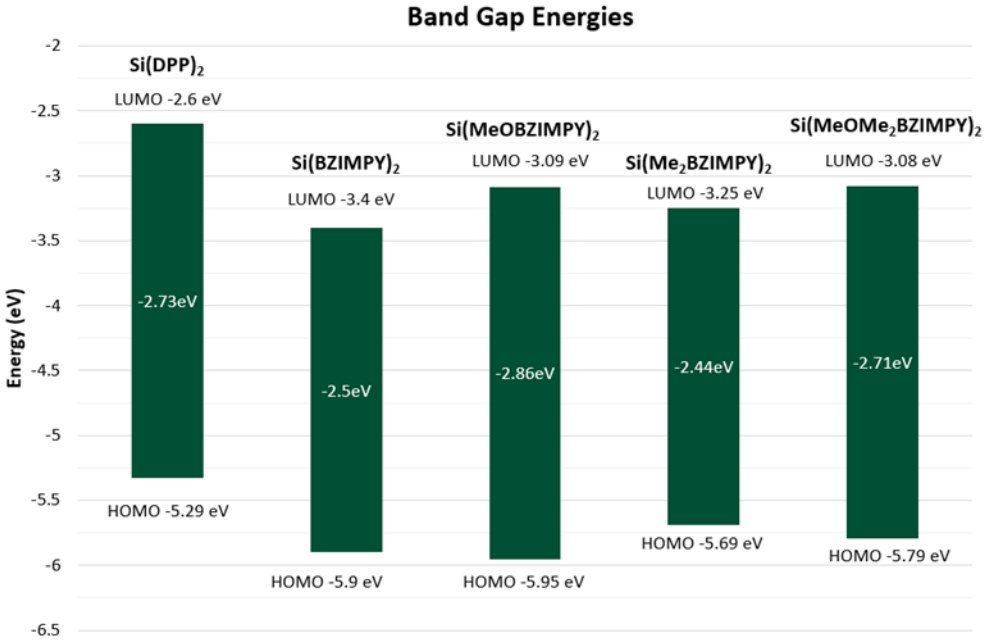

Figure 33: *A comparative band edge diagram of $Si(DPP)_2$ and $Si(bzimpy)_2$ analogs.* [50,53]

Furthemore, the advantage of $Si(DPP)_2$ is even more clear when comparing the mobility values (**Table 4**). Note that previous attempts to raise the LUMO by placing electron donating substitutents on the pyiridine were successful as seen in **Figure 33**, but the modification greatly impacted the mobility by several orders of magnitude to a negative extent. Replacing the NNN-pincer ligand with the DPP pincer ligand simulateously achieved the desired LUMO-raising effect while also increasing the electron mobility of the complex – a win-win for ETL applications.

Table 4: *Si(bzimpy)2 analogs and Si(DPP)2 charge mobilities.*[50,53]

Complex	μ_e (cm^2/Vs)	μ_h (cm^2/Vs)
$Si(MeObzimpy)_2$	2.51×10^{-8}	1.76×10^{-8}
$Si(MeOMe_2bzimpy)_2$	4.89×10^{-7}	3.19×10^{-8}
$Si(Me_2bzimpy)_2$	2.94×10^{-5}	1.44×10^{-6}
$Si(bzimpy)_2$	9.68×10^{-5}	5.31×10^{-6}
$Si(DPP)_2$	1.8×10^{-4}	1.1×10^{-5}

Finally, $Si(DPP)_2$ compares well to the industy grade transport materials currently used by OLED manufacturers (**Table 5**). $Si(DPP)_2$ shows as a very promising electron transport material, having the second highest mobility, falling under BPhen which has the highest at $52x10^{-5}$ cm^2/Vs and a very high T_g. However, as mentioned previously, the LUMO still needs to be raised more and the bandgap increased to be useful for TADF enabled devices.

Table 5: *ETL materials comparison with $Si(DPP)_2$. Problematic properties highlighted in red.*[18-29,53]

	Stability or purity issues	Retail price ($/g)	e^- mobility ($x10^{-5}cm^2/Vs$)	LUMO (eV)	T_1, triplet exciton (eV)	T_g or MP (°C)
Alq_3	Isomerizes	45	0.4 -1.1	-2.9	2.1	175
T2T	Stable	1034	12	-3.0	2.8	55
BPhen	Stable	108	52	-3.0	2.5	66
TPBi	Stable	566	3.3-8.0	-2.7	2.7	122
$Si(DPP)_2$	Stable	?	18	-2.6	<2.6	262

3.3 Experimental details

Thin film devices were grown by Tyler Adams under the direction of Professor Michael Walter. Experimental details of the film growth are included.

Construction of devices for SCLC measurement: ITO patterned glass substrates (Ossila) were sonicated sequentially in DI water, acetone, and isopropyl alcohol for 15 min, dried with N_2, and

treated with UV ozone etch for 20 min. Silicon complexes and aluminum or gold contact electrodes were thermally deposited at 10^{-6} mbar pressure using tungsten evaporation boats. Devices for measuring hole mobilities were constructed by depositing the silicon complexes onto PEDOT:PSS-coated ITO electrodes followed by Au thermal evaporation. PEDOT:PSS films S3 were prepared by filtering PEDOT:PSS solutions through a 0.45 μm PTFE filter. The filtered solution and ITO electrode was heated to 75 °C for 15 min prior to spin coating. The PEDOT:PSS solution was deposited using spin coating (90 mL of solution onto the substrate at 5000 RPM for 50s). PEDOT:PSS was removed from the side ITO conductive strips on the patterned electrodes using water, and the films were annealed at 130 °C for 15 min on a hot plate at ambient conditions. Silicon complexes were thermally deposited onto the PEDOT-coated ITO electrodes at 0.2 Å s-1 (173 nm) and Au was deposited at 0.1-0.3 Å s-1 (50 nm). Devices for measuring electron mobilities were constructed in an ITO/Silicon complex/Al configuration. The patterned ITO glass substrates (Ossila) were sonicated sequentially in DI water, acetone, and isopropyl alcohol for 15 min, dried with N2, and treated with UV ozone etch for 20 min. The silicon complex and aluminum contact electrodes were thermally deposited at 10-6 mbar pressure using tungsten evaporation boats. The 100 nm of silicon complex was deposited at a rate of 0.2 A/s and the 150 nm of aluminum was deposited at a rate of 0.3 A/s.

Chapter 4: Conclusions and future work

In this work the attempted syntheses of three hypercoordinate silicon complexes were discussed; both pentacoordinate complexes proved too prone to decomposition to fully characterize or to study in devices. In contrast, the hexacoordinate $Si(DPP)_2$ complex was found to be both air and water stable and is the first SiC4N2 compound with a Si-N bond length in the conventional range of 2.0 Å or less (1.91 Å). Additionally, this complex proved to be thermally stable to temperatures above 400 °C with a remarkably high T_g onset (263 °C). The complex was thermally evaporated and deposited in thin films to be studied in devices. The hole mobility of the σ delocalized HOMO and the electron mobility of the π delocalized LUMO of $Si(DPP)_2$ are roughly matched, suggesting this complex and other similar $Si(CNC)_2$ complexes could be strong candidates for bipolar charge transport layers in organic electrons. Specifically, $Si(DPP)_2$ is also a strong candidate to act as an electron transport layer, as the comparison with other transport layers shows.

One consistant issue with the $Si(DPP)_2$ complex has been the low yield and turn around time. This suggests that there is futher work to be done in optimizing the overall synthesis of the $Si(DPP)_2$ complex. Another issue is that the LUMO is low compared to current ETL materials and needs to be raised. As with the $Si(bzimpy)_2$ motif, $Si(DPP)_2$ can potentially have substituents added to the pincer to change electronic properties of the overall complex. However, although addition of electron donating groups to the $Si(bzimpy)_2$ platform did raise the band gaps as expected, the addition of the electron donating substituents reduced the electron mobility by orders of magnitude. This result suggests the better strategy for tuning the band edges may be through judicious design of the heterocycles in the pincer ligands instead.

Preliminary research is undeway with other targeted pincer ligands to expand the range of Si(pincer)$_2$ HOMO-LUMO tuning and to meet the various needs of different organic electronic device applications (**Figure 34**). **FT1**, the pyrazine analog to Si(DPP)$_2$, is an attractive target for lowering the LUMO for ETLs better matched for electron injection from silver printed cathodes. This N-rich analog to Si(DPP)$_2$ is being synthesized using similar methods, but starting with 2,6-dibromopyrazine instead of 2,6-dibromopyridine. Preliminairy evidence of **FT1** via mass spec indicates the route developed for Si(DPP)$_2$ is compatible for the pyrazine analog. Further development is needed though to fully characterize the product and to incorporate the complex into devices with silver electrodes.

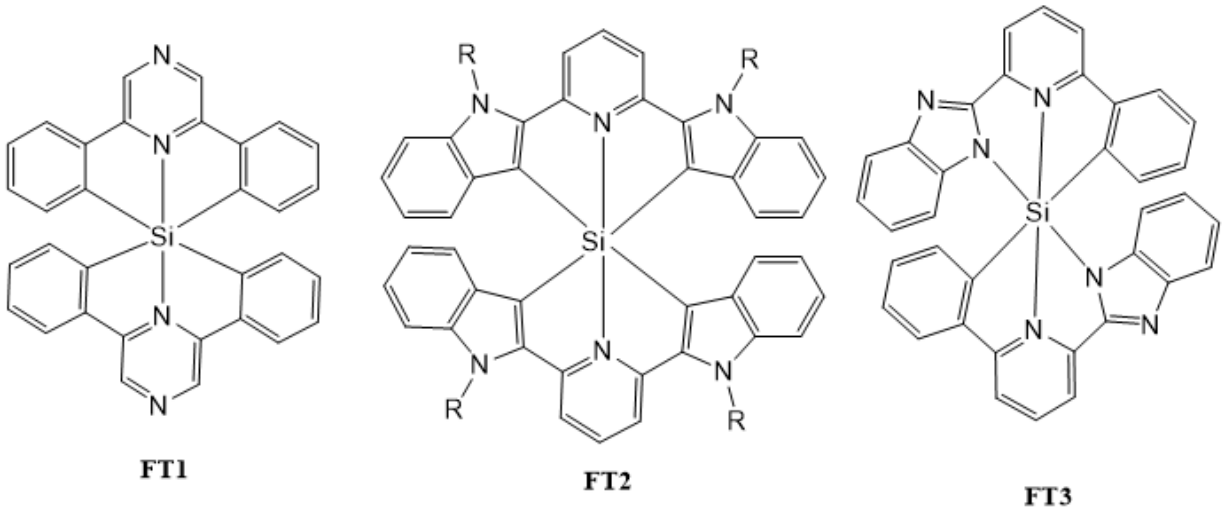

Figure 34: *Future synthetic targets.*

For greater solution processability, N-alkylate benzamadizole analogs such as **FT2**, where the R group is a saturated aliphatic (e.g. butyl or 2-ethylhexyl) are being developed. **FT2** is expected to retain many of the material, optical, and electronic properties of Si(DPP)$_2$; however, the HOMO is predicted to be σ delocalized. We anticipate that this may lead to a higher hole mobility for **FT2** relative to Si(DPP)$_2$. More importantly, we anticipate the aliphatic

substituents will help solubilize **FT2** enough to enable solution-processible device fabrication methods, including spin-coating, printing and eventually roll-to-roll processing.

Finally, methods developed in this thesis are also being modified to explore asymmetric CNN-pincers like the imidazole-pyridine-phenyl ligand shown in **FT3**. **FT3** is expected to posses ETL properties similar to $Si(bzimpy)_2$ and $Si(DPP)_2$. However, **t**he reduction of symmetry provided by this ligand system and analogs provides the possibility of introducing greater intraligand charge transfer over the entire ligand for stronger optical transitions (absorbance and fluorescence) perhaps for applications as absorbing ETLs in solar cells. A strategy for the pincer ligand has been developed starting with 6-bromopicolinic acid. Condensation with o-phenylenediamine in polyphosphoric acid followed by a Suzuki coupling with bromophenylboronic acid provides a practical route to the ligand. However, subsequent attempts at lithiation and reaction with $SiCl_4$ have thus far been unsuccessful. Additional studies are needed to realize **FT3** and to expore its optical and electronic properties.

REFERENCES

1. Bernanose, A.; Vouaux, P. Électroluminescence organique : étude du mode d'émission. *J. Chim. Phys*. **1953**, *50*, 261-263.
2. Pope, M.; Kallmann, H. P.; Magnante, P. Electroluminescence in Organic Crystals. The *J. Chem. Phys.* **1963**, *38* (8), 2042-2043
3. Zou, S.-J.; Shen, Y.; Xie, F.-M.; Chen, J.-D.; Li, Y.-Q.; Tang, J.-X. Recent advances in organic light-emitting diodes: toward smart lighting and displays. *Mater. Chem. Front.*, **2020**, *4* (3), 788-820.
4. Hung, L. S.; Chen, C. H. Recent progress of molecular organic electroluminescent materials and devices *Mater. Sci. Eng., R*, **2002**, *39*, 143
5. Abdulrazzaq, O. A.; Saini, V.; Bourdo, S.; Dervishi, E.; Biris, A. S. Organic Solar Cells: A Review of Materials, Limitations, and Possibilities for Improvement. *Part. Sci. Technol.* **2013**, *31* (5), 427-442.
6. Facchetti, A. Semiconductors for organic transistors. *Mater. Today.* **2007**, *10* (3), 28-37.
7. Mertens, R. The OLED Handbook. A Guide to OLED Technology, Industy & Market. OLED-Info: **2019**; p. 145.
8. Jou, J. H.; Kumar, S.; Agrawal, A.; Li, T. H.; Sahoo, S. Approaches for fabricating high efficiency organic light emitting diodes. *J. Mater. Chem. C.* **2015**, *3* (13), 2974-3002
9. Kocherga, M. Hexacoordinate silicon complexes for electronic devices. Ph.D. Dissertation. University of North Carolina, Charlotte, NC, 2020.
10. Song, J.; Lee, H.; Jeong, E. G.; Choi, K. C.; and Yoo, S. Organic Light-Emitting Diodes: Pushing Toward the Limits and Beyond, *Adv. Mater*. **2020**, *32*(*35*), 1907539.

11. Liu, H.; Ma, Z.; Yu, R.; Gao, H.; Lin, J.; Hayat, T.; Alsaedi, A.; and Tan, Z. A. Crosslinkable metal chelate as the electron transport layer for efficient and stable inverted polymer solar cells, *Mater. Chem. Front*. **2020**, *4*(*10*), 2995–3002.
12. Chen C. H.; and Shi, J. Metal chelates as emitting materials for organic electroluminescence, *Coord. Chem. Rev*. **1998**, *171*, 161–174.
13. Evans, R. C.; Douglas, P.; and Winscom, C. J. Coordination complexes exhibiting room-temperature phosphorescence: Evaluation of their suitability as triplet emitters in organic light emitting diodes, *Coord. Chem. Rev*. **2006**, *250*(*15*), 2093–2126.
14. Yersin, H.; Rausch, A. F.; Czerwieniec, R.; Hofbeck, T.; and Fischer, T. The triplet state of organo-transition metal compounds. Triplet harvesting and singlet harvesting for efficient OLEDs, *Coord. Chem. Rev*. **2011**, *255*(*21*), 2622–2652
15. Tsuboyama, A.; Iwawaki, H.; Furugori, M.; Mukaide, T.; Kamatani, J.; Igawa, S.; Moriyama, T.; Miura, S.; Takiguchi, T.; Okada, S.; Hoshino, M.; and Ueno, K. Homoleptic Cyclometalated Iridium Complexes with Highly Efficient Red Phosphorescence and Application to Organic Light-Emitting Diode, *J. Am. Chem. Soc*. **2003**, *125*(*42*), 12971–12979
16. Zhang, Q.; Li, B.; Huang, S.; Nomura, H.; Tanaka, H.; and Adachi, C. Efficient blue organic light-emitting diodes employing thermally activated delayed fluorescence, *Nat. Photonics* **2014**, *8*(*4*), 326–332.
17. Zhang, Q.; Li, J.; Shizu, K.; Huang, S.; Hirata, S.; Miyazaki H.; and Adachi, C. Design of Efficient Thermally Activated Delayed Fluorescence Materials for Pure Blue Organic Light Emitting Diodes, *J. Am. Chem. Soc*. **2012**, *134*(*36*), 14706–14709.

18. Juang, F. S.; Lee, C. C.; Chen, J. Y.; Lin, Y. H.; and Zhang, D. W. Lifetime study for solution processed organic light emitting diodes, *IOP Conf. Ser.: Mater. Sci. Eng*. **2019**, *600*, 012018.

19. Burrows, H. D.; Fernandes, M.; de Melo, J. S.; Monkman, A. P.; Navaratnam, S. Characterization of the triplet state of tris(8-hydroxyquinoline)aluminium(III) in benzene solution. *J. Am. Chem. Soc.* **2003,** *125* (50), 15310-15311.

20. Mayr, C.; Brutting, W. Control of Molecular Dye Orientation in Organic Luminescent Films by the Glass Transition Temperature of the Host Material. *Chem. Mater.* **2015,** *27* (8), 2759-2762.

21. Chen, H. F.; Yang, S. J.; Tsai, Z. H.; Hung, W. Y.; Wang, T. C.; Wong, K. T. 1,3,5-Triazine derivatives as new electron transport-type host materials for highly efficient green phosphorescent OLEDs. *J. Mater. Chem.* **2009,** *19* (43), 8112-8118.

22. Tsang, D. P. K.; Adachi, C. Operational stability enhancement in organic light-emitting diodes with ultrathin LiQ interlayers. *Sci. Rep.* **2016,** *6*.

23. Yadav, R. A. K.; Dubey, D. K.; Chen, S. Z.; Liang, T. W.; Jou, J. H. Role of Molecular Orbital Energy Levels in OLED Performance. *Sci. Rep.* **2020,** *10* (1).

24. Xin, Q.; Li, W. L.; Su, W. M.; Li, T. L.; Su, Z. S.; Chu, B.; Li, B. Emission mechanism in organic light-emitting devices comprising a europium complex as emitter and an electron transporting material as host. *J. Appl. Phys.* **2007,** *101* (4).

25. Choi, Y. H.; Jeon, Y. P.; Choo, D. C.; Kim, T. W. Enhancement of out-coupling efficiency due to an organic scattering layer in organic light-emitting devices. *Org. Electron.* **2015,** *22*, 197-201.

26. Juang, F.-S.; Lee, C. C.; Chen J. Y.; Lin, Y. H.; Zhang, D. W. Lifetime study for solution processed organic light emitting diodes *IOP Conf. Ser.: Mater. Sci. Eng*. **2019,** *600*, 012018.

27. Shi, W. X.; Liu, N.; Zhou, Y. M.; Cao, X. A. Effects of Postannealing on the Characteristics and Reliability of Polyfluorene Organic Light-Emitting Diodes. *IEEE T. Electron Dev.* **2019,** *66* (2), 1057-1062.

28. Takizawa, S. Y.; Montes, V. A.; Anzenbacher, P. Phenylbenzimidazole-Based New Bipolar Host Materials for Efficient Phosphorescent Organic Light-Emitting Diodes. *Chem. Mater.* **2009,** *21* (12), 2452-2458.

29. Wang, Z. M.; Lu, P.; Chen, S. M.; Gao, Z.; Shen, F. Z.; Zhang, W. S.; Xu, Y. X.; Kwok, H. S.; Ma, Y. G. Phenanthro 9,10-d imidazole as a new building block for blue light emitting materials. *J. Mater. Chem.* **2011,** *21* (14), 5451-5456.

30. Voronkov, M. G. Silatranes: intra-complex heterocyclic compounds of pentacoordinated silicon. *Pure Appl. Chem.* **1966,** *13* (1-2), 35-59.

31. Voronkov, M. G.; D'Yakov, V. M.; Kirpichenko, S. V. Silatranes. *J. Organomet. Chem.* **1982,** *233* (1), 1-147.

32. Frye, C. L.; Vincent, G. A.; Finzel, W. A. Pentacoordinate silicon compounds. V. Novel silatrane chemistry. *J. Am. Chem. Soc.* **1971,** *93* (25), 6805-11.

33. Chandrasekaran, A.; Day, R. O.; Holmes, R. R. A New Class of Silatranes: Structure and Dynamic NMR Behavior. *J. Am. Chem. Soc.* **2000,** *122* (6), 1066-1072.

34. Puri, J. K.; Singh, R.; Chahal, V. K. Silatranes: a review on their synthesis, structure, reactivity and applications. *Chem. Soc. Rev.* **2011,** *40* (3), 1791-1840.

35. Singh, G.; Kaur, G.; Singh, J. Progressions in hyper-coordinate silicon complexes. *Inorg. Chem. Commun.* **2018,** *88*, 11-20.

36. Riggleman, S.; DeShong, P. Application of Silicon-Based Cross-Coupling Technology to Triflates. *J. Org. Chem.* **2003,** *68* (21), 8106-8109.

37. Shlyakhtenko, L. S.; Gall, A. A.; Filonov, A.; Cerovac, Z.; Lushnikov, A.; Lyubchenko, Y. L. Silatrane-based surface chemistry for immobilization of DNA, protein-DNA complexes and other biological materials. *Ultramicroscopy* **2003,** *97* (1-4), 279-287.

38. A select pharmaceutical review (a) Voronkov, M. G. Biological activity of silatranes. *Top. Curr. Chem.* **1979**, *84*, 77-135. (b) Voronkov, M. G.; Baryshok, V. P., Antitumor activity of silatranes. *Pharm. Chem. J. (Translation of Khimiko-Farmatsevticheskii Zhurnal)* **2004**, *38* (1), 3-9.

39. Allen, C. M.; Sharman, W. M.; Van Lier, J. E. Current status of phthalocyanines in the photodynamic therapy of cancer. *J. Porphyr. Phthalocyanines.* **2001**, *5* (2), 161-169.

40. Melville, O. A.; Grant, T. M.; Mirka, B.; Boileau, N. T.; Park, J.; Lessard, B. H. Ambipolarity and Air Stability of Silicon Phthalocyanine Organic Thin-Film Transistors. *Adv. Electron. Mater.* **2019**, *5* (8).

41. Boyer-Elma, K.; Carre, F. H.; Corriu, R. J. P.; Douglas, W. E. Preparation of a diethynyl hypervalent silicon monomer by coordination-selective cleavage - structure and polymerization to give novel polycarbosilanes containing main-chain hexacoordinate silicon. *J. Chem. Soc., Chem. commun.* **1995**, (*7*), 725-726.

42. Coles, M. P.; Khalaf, M. S.; Hitchcock, P. B. A new aliphatic N,C,N'-pincer ligand with pendant guanidine groups. *Inorganica Chim. Acta.* **2014**, *422*, 228-234.

43. Belzner, J.; Ihmels, H.; Kneisel, B. O.; Gould, R. O.; Herbstirmer, R. Reactions of a cyclotrisilane with olefins and dienes - evidence for an equilibrium between silylenes and a cyclotrisilane. *Organometallics* **1995**, *14* (1), 305-311.

44. Peloquin, D. M.; Schmedake, T. A. Recent advances in hexacoordinate silicon with pyridine-containing ligands: Chemistry and emerging applications. *Coord. Chem. Rev*. **2016**, *323*, 107-119.

45. Kawamoto, K.; Akashi, H.; Yamasaki, M.; Shibahara, T. Fluorescent Fluoro-Silicon(IV) Complexes with Schiff Base Ligands *Chem. Lett*. **2013**, *42*, 389–391.

46. Portius, P.; Filippou, A. C.; Schnakenburg, G.; Davis, M.; Wehrstedt, K. D. Neutral Lewis Base Adducts of Silicon Tetraazide *Angew. Chem. Int. Ed*. **2010**, *49*, 8013–8016 (S8013/8011-S8013/8041).

47. Xiang, Y.G.; Fu, C.; Breiding, T.; Sasmal, P.K.; Liu, H.D.; Shen, Q.; Harms, K.; Zhang, L.L.; Meggers, E. Hydrolytically stable octahedral silicon complexes as bioactive scaffolds: application to the design of DNA intercalators. *Chem. Commun*. **2012**, *48* 7131–7133.

48. Peloquin, D.M.; Dewitt, D.R.; Patel, S.S.; Merkert, J.W.; Donovan-Merkert, B.T.; Schmedake, T. A. Spectroelectrochemistry of tris(bipyridyl)silicon(IV): ligand localized reductions with potential electrochromic applications. *Dalton Trans*. **2015**, *44*, 18723–18726.

49. Kocherga, M.; Castaneda, J.; Walter, M. G.; Zhang, Y.; Saleh, N.; Wang, L.; Jones, D. S.; Merkert, J. W.; Donovan-Merkert, B. T.; Li, Y.; Hofmann, T.; and Schmedake, T. A. Si(bzimpy)2 – A hexacoordinate silicon pincer complex for electron transport and electroluminescence *Chem. Commun*. **2018**, *54*, 14073-14076.

50. Kocherga, M.; Boyle, K.; Merkert, J. W.; Schmedake, T.A.; and Walter, M. G. Exploring the molecular electronic device applications of synthetically versatile silicon pincer

complexes as charge transport and electroluminescent layers. *Mater. Adv*., **2022**, *3*, 2373-2379

51. Li, Z.; Jiao, B.; Wu, Z.; Liu, P.; Ma, L.; Lei, X.; Wang, D.; Zhou, G.; Hu, H.; and Hou, X. J. Fluorinated 9,9′-spirobifluorene derivatives as host materials for highly efficient blue organic light-emitting devices. *Mater. Chem. C.* **2013**, *1*, 2183
52. Wan R.; Buss J. A.; Horak, K. T.; and Agapie, T. A hemilabile diphosphine pyridine pincer ligand: σ- and π-binding in molybdenum coordination complexes. *Polyhedron* **2020**, *187*, 114631.
53. Earnhardt, A.W.; Boyle, K.M.; Adams, T.; Walter, M. G.; Wang, Y., Zhang, Y.; Adeyemi, A.; Merkert, J.; Bimukhanov, A. N.; Aldongarov, A. A.; McMillen, C. D.; and Schmedake, T. A. Bipolar charge transport in a robust hexacoordinate Organosilane. *J. Organomet. Chem*., **2022**, *961*, 122208
54. Jia, W. L.; Liu, Q. D.; Wang, R. Y.; Wang, S. N. Novel phosphorescent cyclometalated organotin(IV) and organolead(IV) complexes of 2,6-bis(2 '-indolyl)pyridine and 2,6-bis 2 '-(7-azaindolyl) pyridine. *Organometallics* **2003,** *22* (20), 4070-4078.
55. Parr, R.G.; Yang, W. *Density-functional theory of atoms and molecules*, Oxford Univ. Press, Oxford **1989**.
56. Salahub, D.R.; Zerner, M.C. *The challenge of d and f electrons: theory and computation*, American Chemical Society, Washington D.C. 1989
57. Kohn, W.; and Sham L.J. Self-consistent equations including exchange and correlation effects *Phys. Rev*. **1965**, *140*
58. Hohenberg, P.; and Kohn W. Inhomogeneous electron gas *Phys. Rev.* **1964**, *136*
59. Becke, A.D. Density-functional thermochemistry. III. The role of exact exchange *J. Chem. Phys.* **1993**, *98*, 5648-5652

60. Lee, C.; Yang, W.; and Parr, R.G. Development of the Colle-Salvetti correlation-energy formula into a functional of the electron density *Phys. Rev. B* **1988**, *37* (*2*), 785-789

61. Miehlich, B.; Savin, A.; Stoll, H.; and Preuss, H. Results obtained with the correlation-energy density functionals of Becke and Lee, Yang and Parr *Chem. Phys. Lett*. **1989**, *157* (*3*), 200-206

62. Rigaku Oxford Diffraction, **CrysAlisPro Software System, Version 1.171.38.46** Rigaku Corporation, Oxford, UK (**2018**)

63. Bruker. *Apex3 v2017.3-0, SAINT V8.38A*; Bruker AXS Inc.: Madison (WI), USA, 2017

64. Sheldrick, G. M. A short history of SHELX, *Acta Crystallogr. A.* **2008**, *64*, 112-122

65. Dolomanov, O.V.; Bourhis, L.J.; Gildea, R.J.; Howard, J.A.K.; and Puschmann, H. OLEX2: a complete structure solution, refinement and analysis program *J. Appl. Cryst*. **2009**, *42*, 339-341

66. Marcus, R. A.; and Sutin, N., Electron transfers in chemistry and biology. *Biochim. Biophys. Acta.* **1985,** *811* (3), 265-322.

67. Coropceanu, V.; Cornil, J.; da Silva, D. A.; Olivier, Y.; Silbey, R.; and Bredas, J. L., Charge transport in organic semiconductors. *Chem. Rev.* **2007,** *107* (*4*), 926-952.

APPENDIX A: ^{1}H NMR spectrum of Si(bzimpy)Me$_2$ in CDCl$_3$

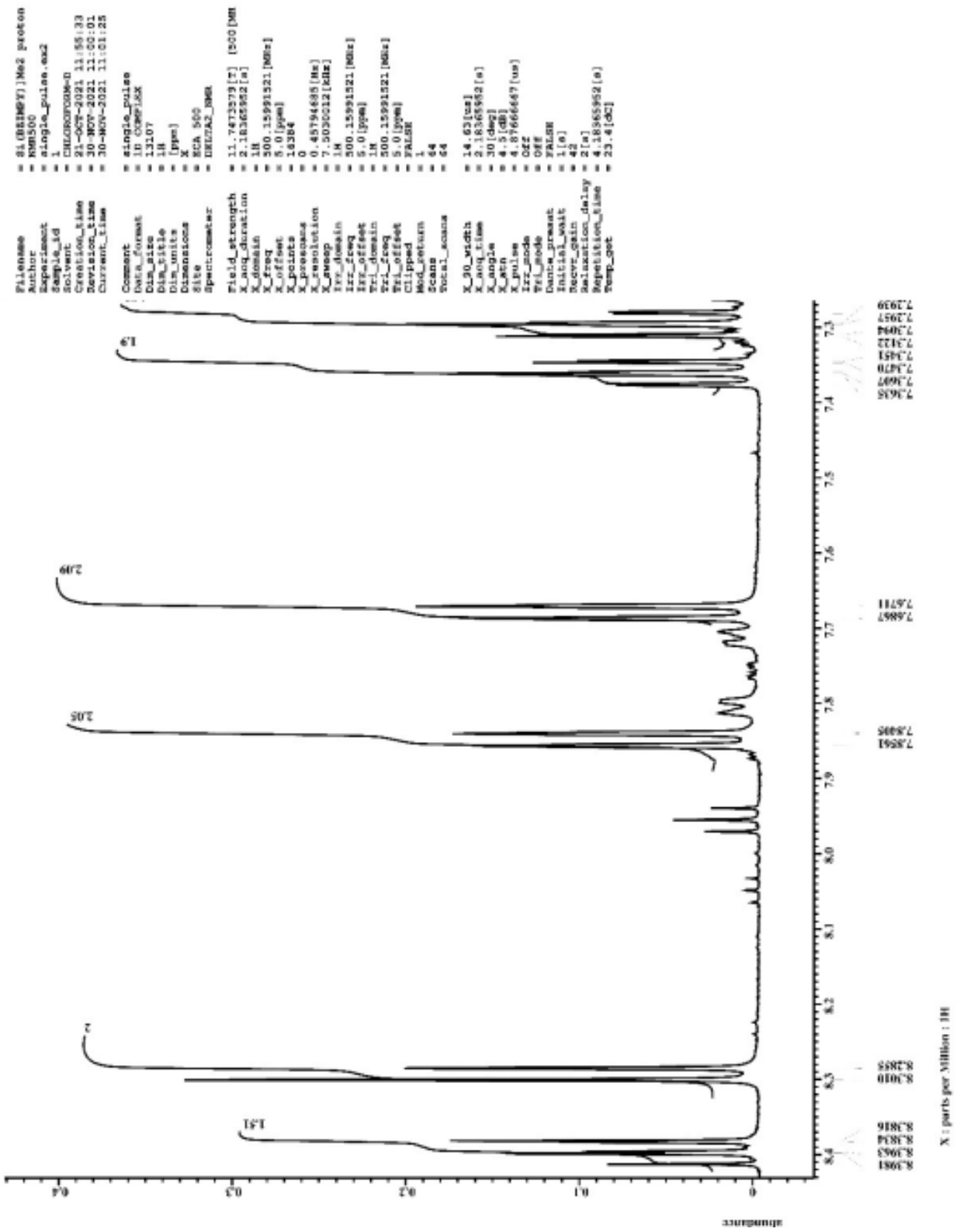

APPENDIX B: ^{1}H NMR full spectrum of Si(bzimpy)Me$_2$ in CDCl$_3$

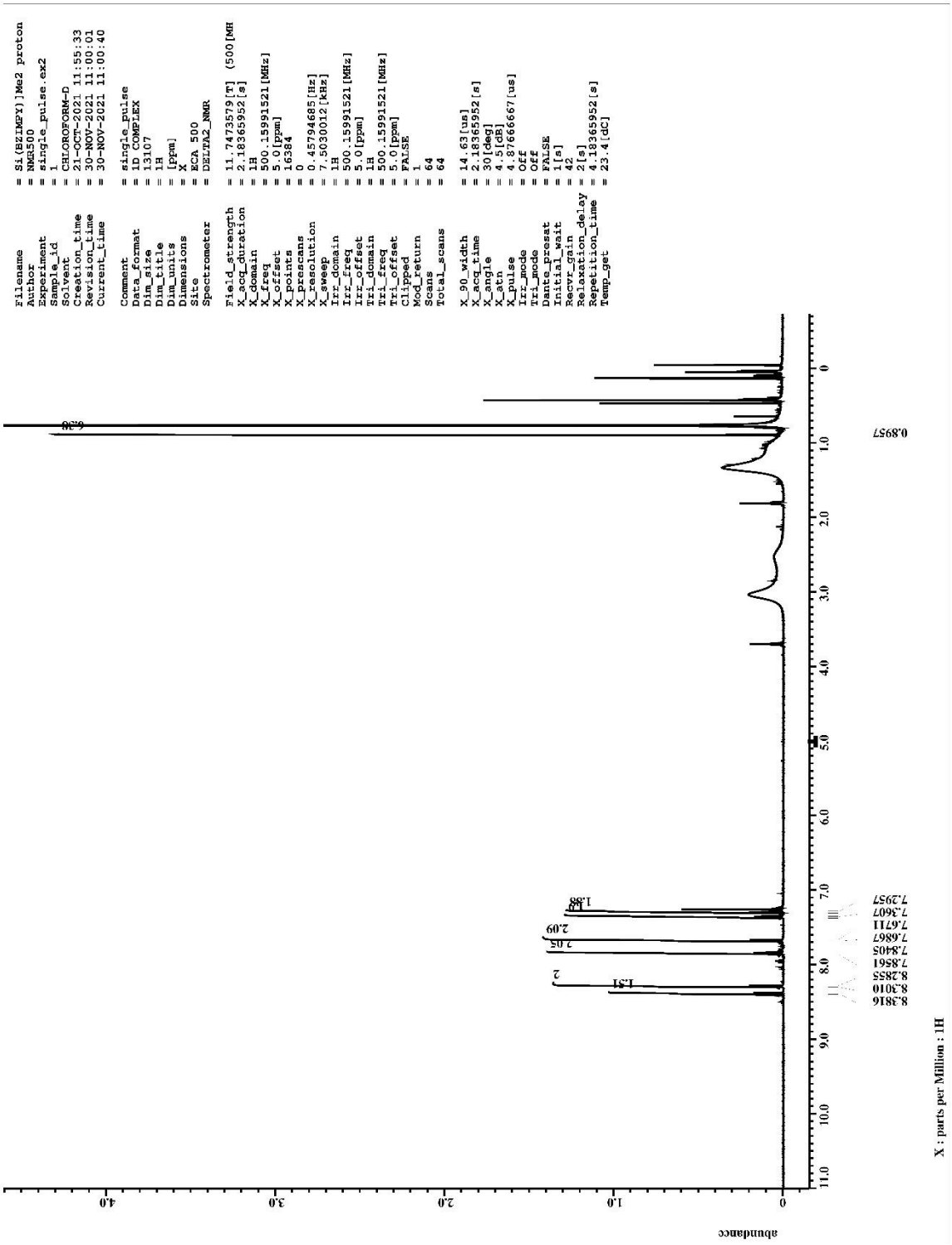

APPENDIX C: ^{13}C NMR spectrum of Si(bzimpy)Me_2 in $CDCl_3$

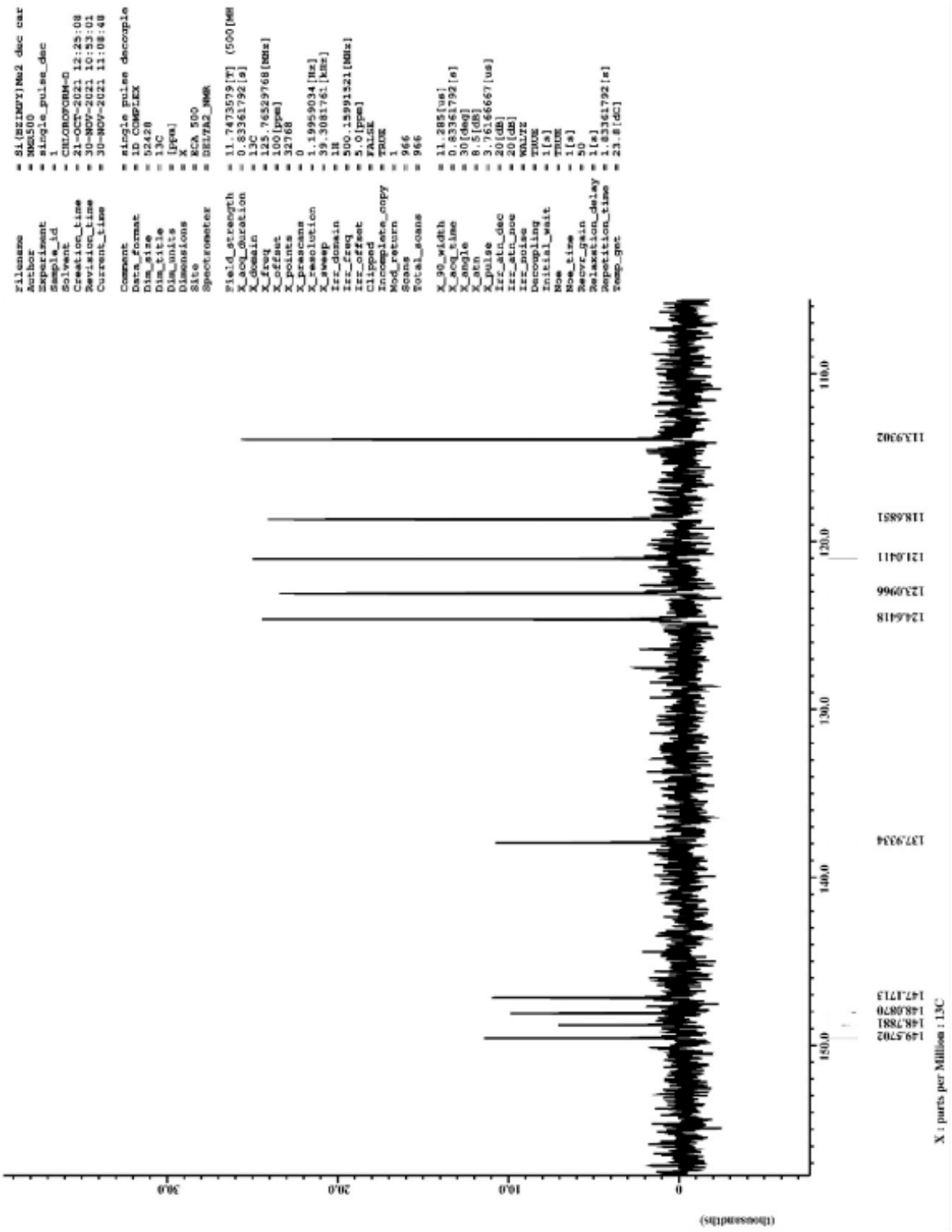

APPENDIX D: ^{29}Si NMR spectrum of Si(bzimpy)Me$_2$ in CDCl$_3$

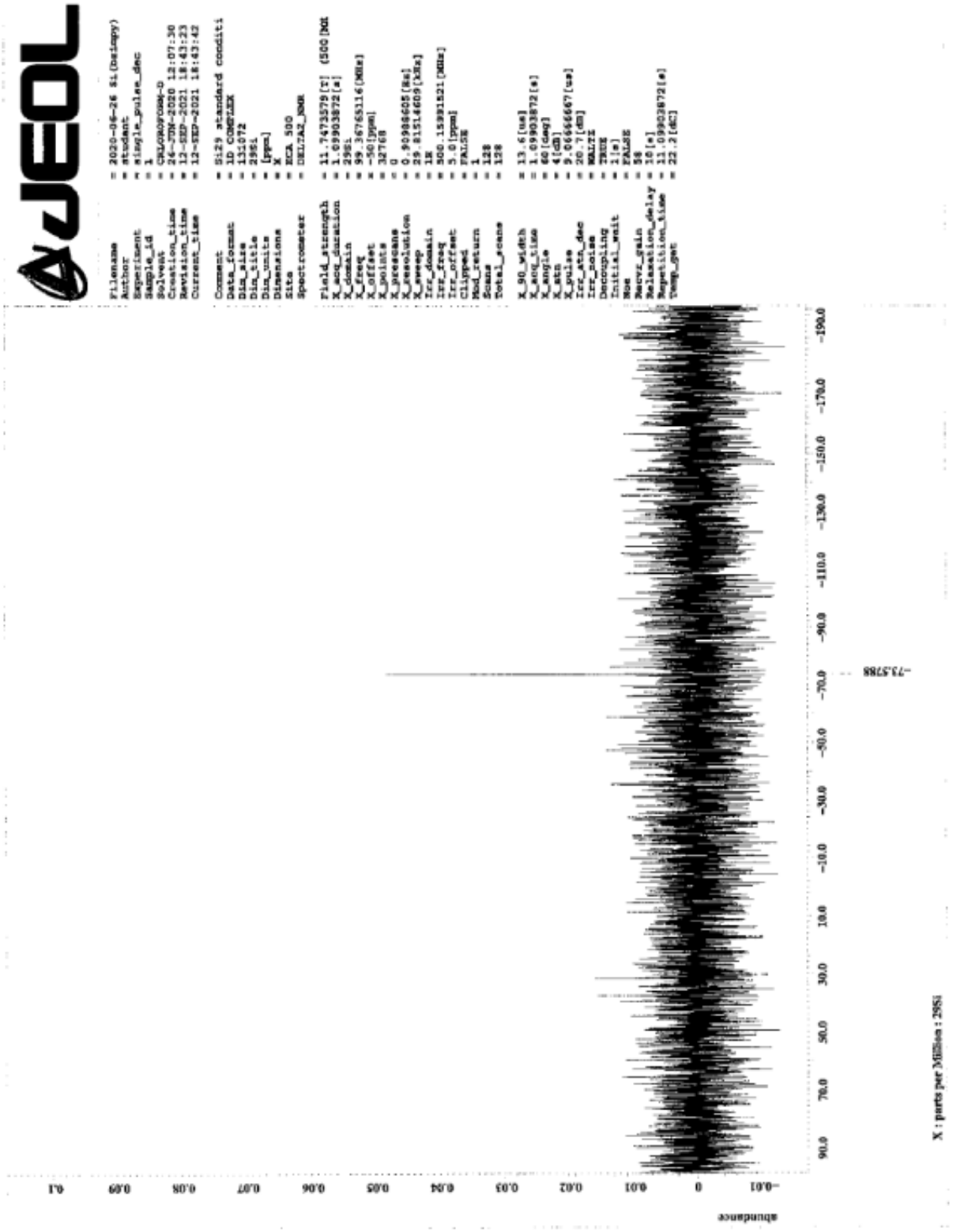

APPENDIX E: MALDI TOF spectrum of Si(bzimpy)Me_2

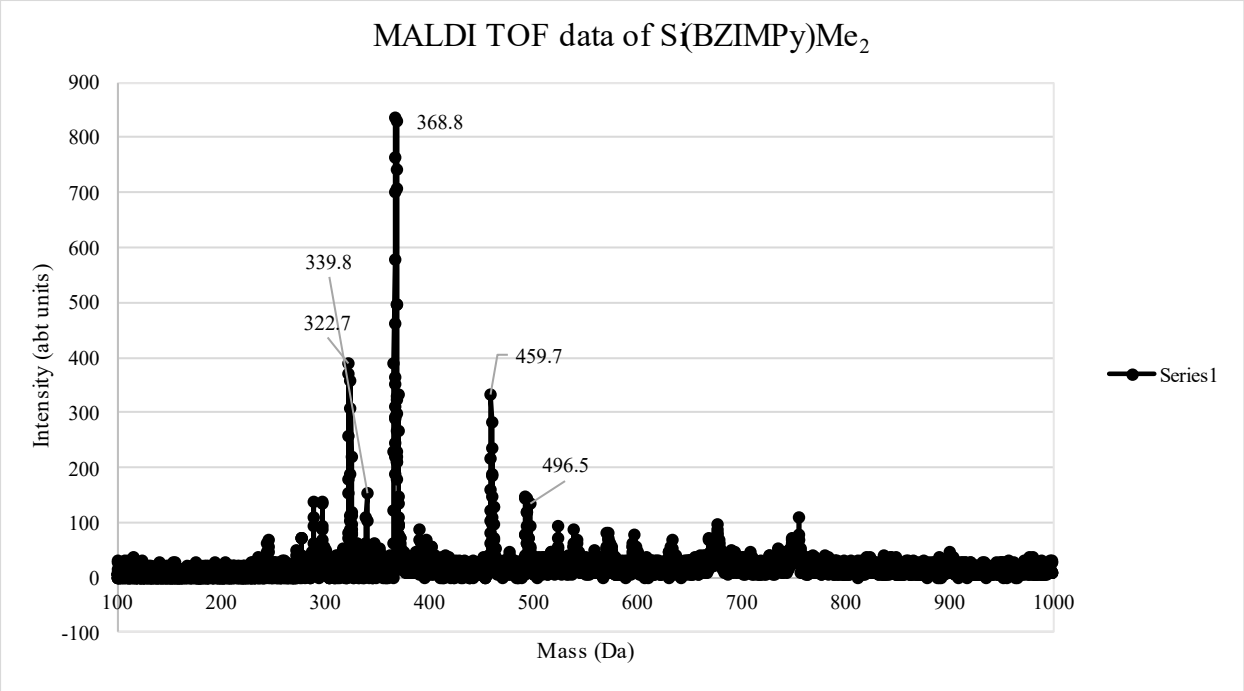

APPENDIX F: Crystallographic data of Si(bzimpy)Me_2

	Si(bzimpy)Me_2*½$CHCl_3$
empirical formula	$C_{21.5}H_{17.5}Cl_{1.5}N_5Si$
formula weight (g/mol)	427.17
crystal system	triclinic
space group, *Z*	*P*-1, 4
temperature (K)	100
wavelength (Å)	1.54184
crystal size (mm)	0.32 x 0.37 x 0.48
a, Å	11.1264(3)
b, Å	12.2430(4)
c, Å	15.6147(4)
α,°	82.157(2)
β, °	86.393(2)
γ, °	64.811(3)
volume ($Å^3$)	1906.75(10)
D_{calc} (g/cm^3)	1.488
abs. coeff. (mm^{-1})	3.176
F(000)	884
Θ range for data	4.02-66.81
reflections collected	33500
data/restraints/parameters	6734 / 0 / 528
R(int)	0.0321
final R [$I > 2\sigma(I)$] R1, wR2	0.0293, 0.0749
final R (all data) R1, wR2	0.0321, 0.0773
goodness-of-fit on F^2	1.031
larg. diff. peak, hole, $eÅ^{-3}$	0.325, -0.346
CCDC Deposition No.	2109550

APPENDIX G: ^{13}C NMR spectrum of $Si(DPP)Me_2$ in CD_2Cl_2

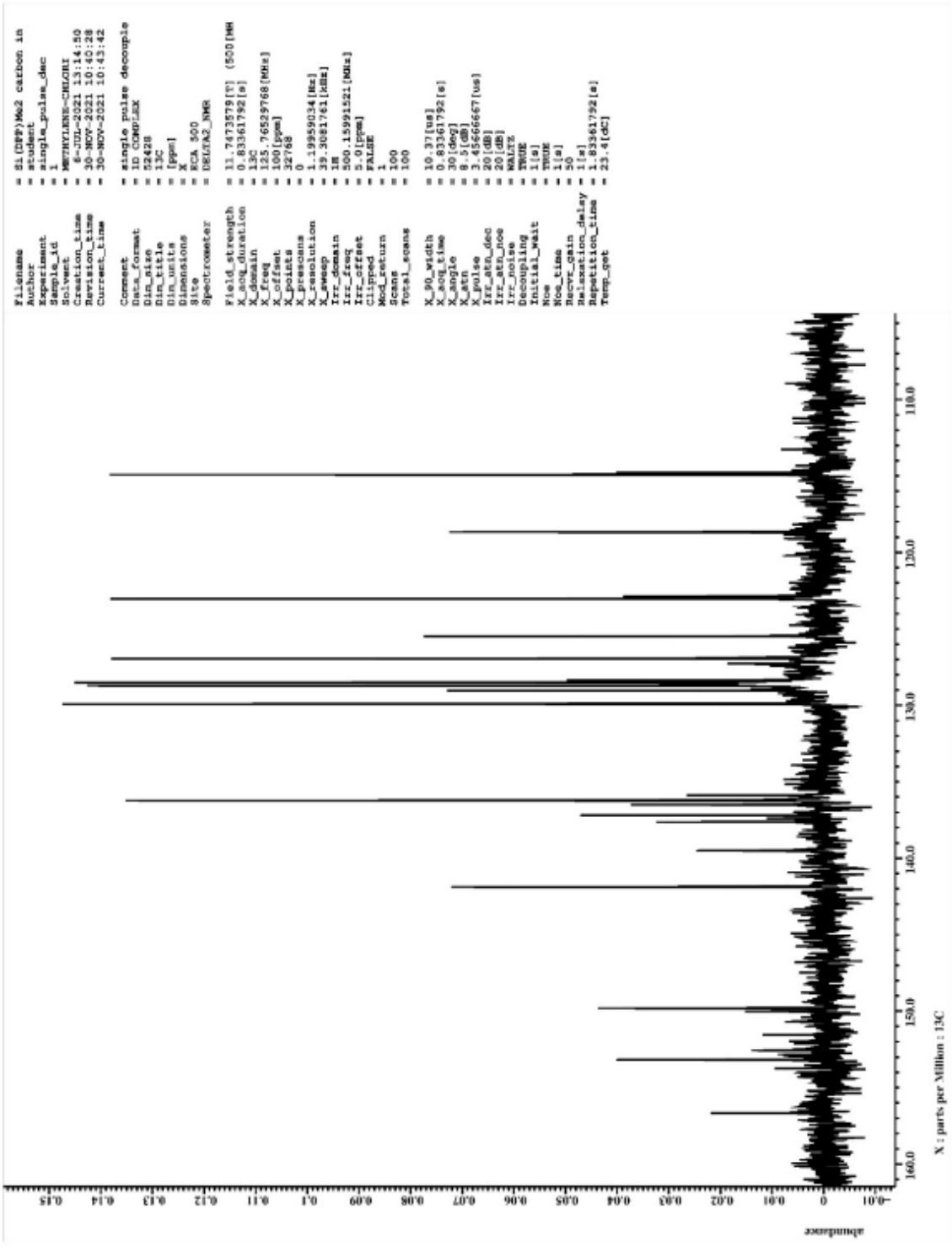

APPENDIX H: ^{29}Si NMR spectrum of $Si(DPP)Me_2$ CD_2Cl_2

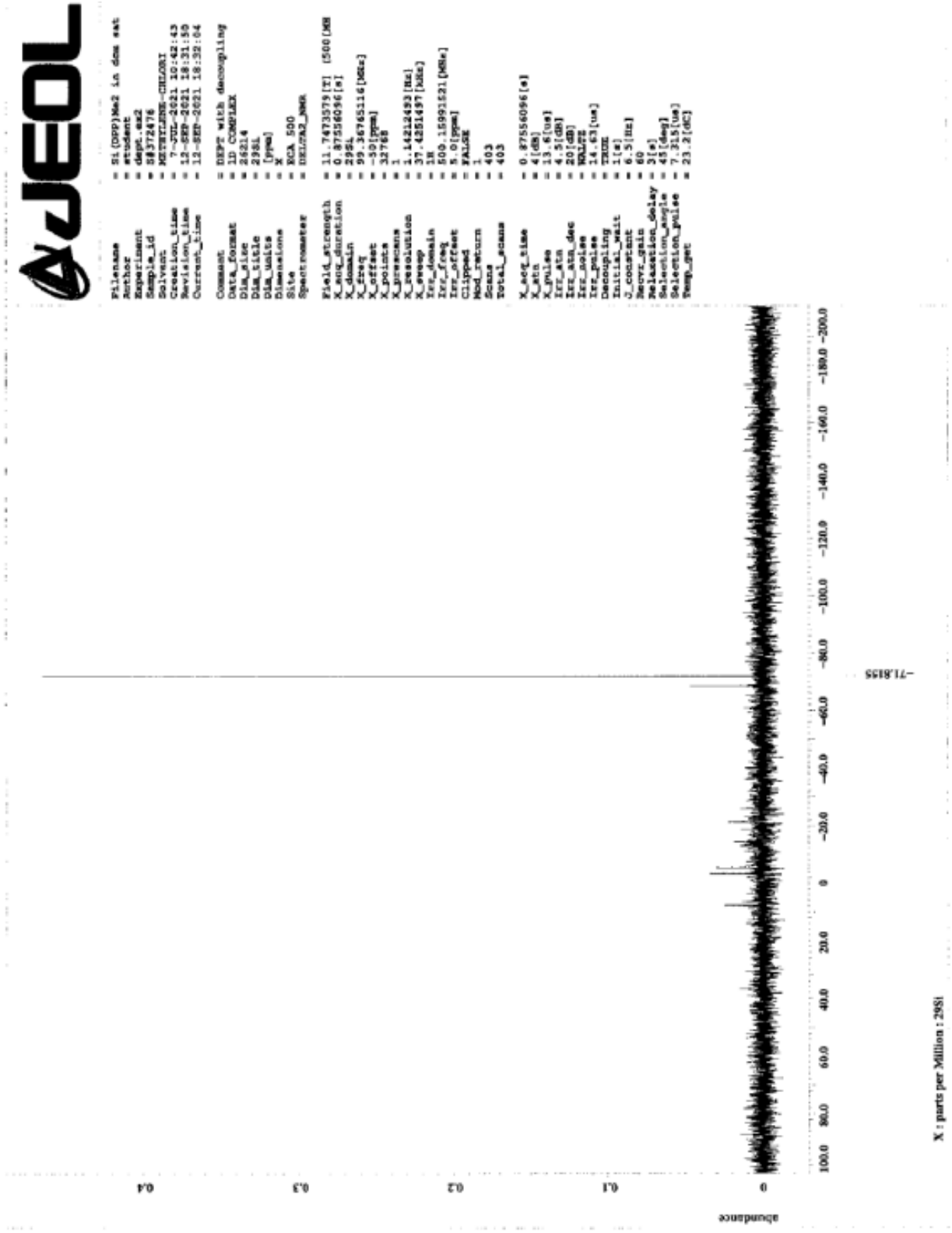

APPENDIX I: MALDI TOF spectrum of $Si(DPP)Me_2$

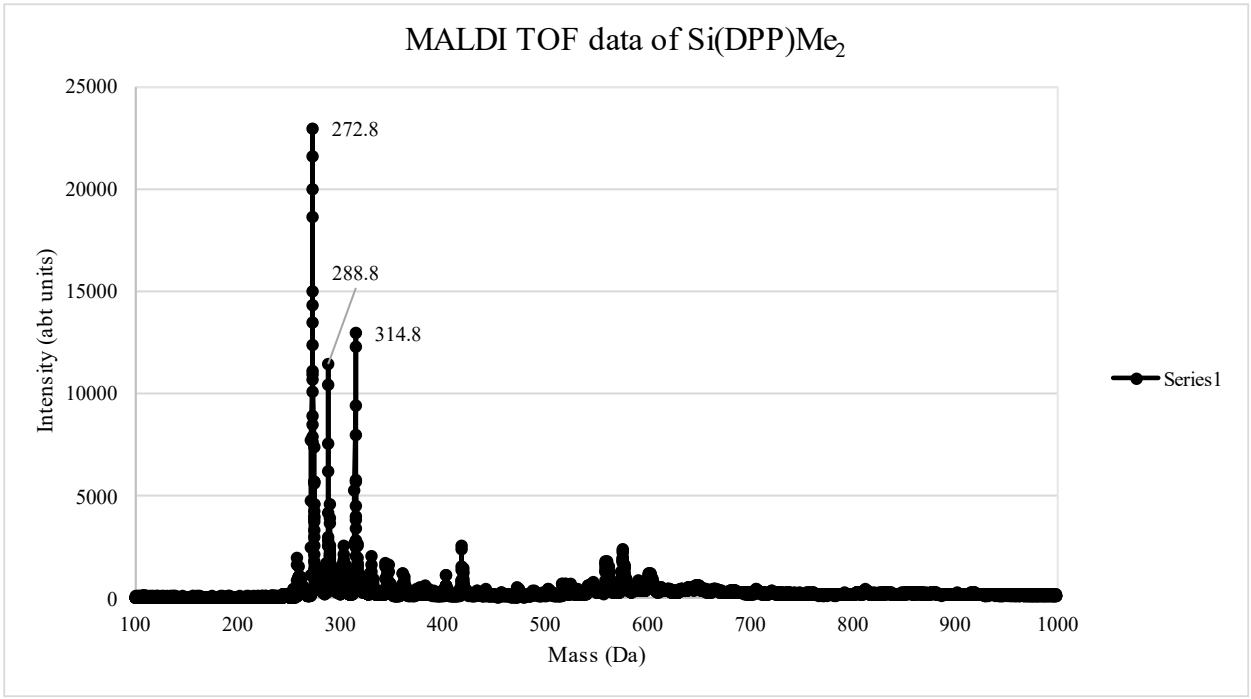

APPENDIX J: Crystallographic data of $Si(DPP)Me_2OSi(DPP)Me_2$

	$Si(DPP)Me_2OSi(DPP)Me_2$
empirical formula	$C_{38}H_{36}N_2OSi_2$
formula weight (g/mol)	592.893
crystal system	triclinic
space group, *Z*	*P*-1
temperature (K)	100
wavelength (Å)	1.54184
crystal size (mm^3)	0.23 x 0.24 x 0.71
a/Å	12.4394(5)
b/Å	12.8631(6)
c/Å	13.0980(6)
α/°	62.367(5)
β/°	62.040(5)
γ/°	87.713(4)
Volume($Å^3$)	1597.25(18)
D_{calc} (g/cm^3)	1.233
abs. coeff. (mm^{-1})	1.256
F(000)	630.6
Θ range for data	7.96 to 133.86°
reflections collected	27517
Data/restraints/parameters	5621/0/393
R(int)	0.0399
final R [$I > 2\sigma(I)$] R1, wR2	0.0377, 0.0947
final R (all data) R1, wR2	0.0455, 0.1021
Goodness-of-fit on F^2	1.054
larg. diff. peak, hole, $eÅ^{-3}$	0.38/-0.39
CCDC Deposition No.	NA

APPENDIX K: ^{1}H NMR spectrum of Si(DPP)$_2$ in DMSO-d$_6$

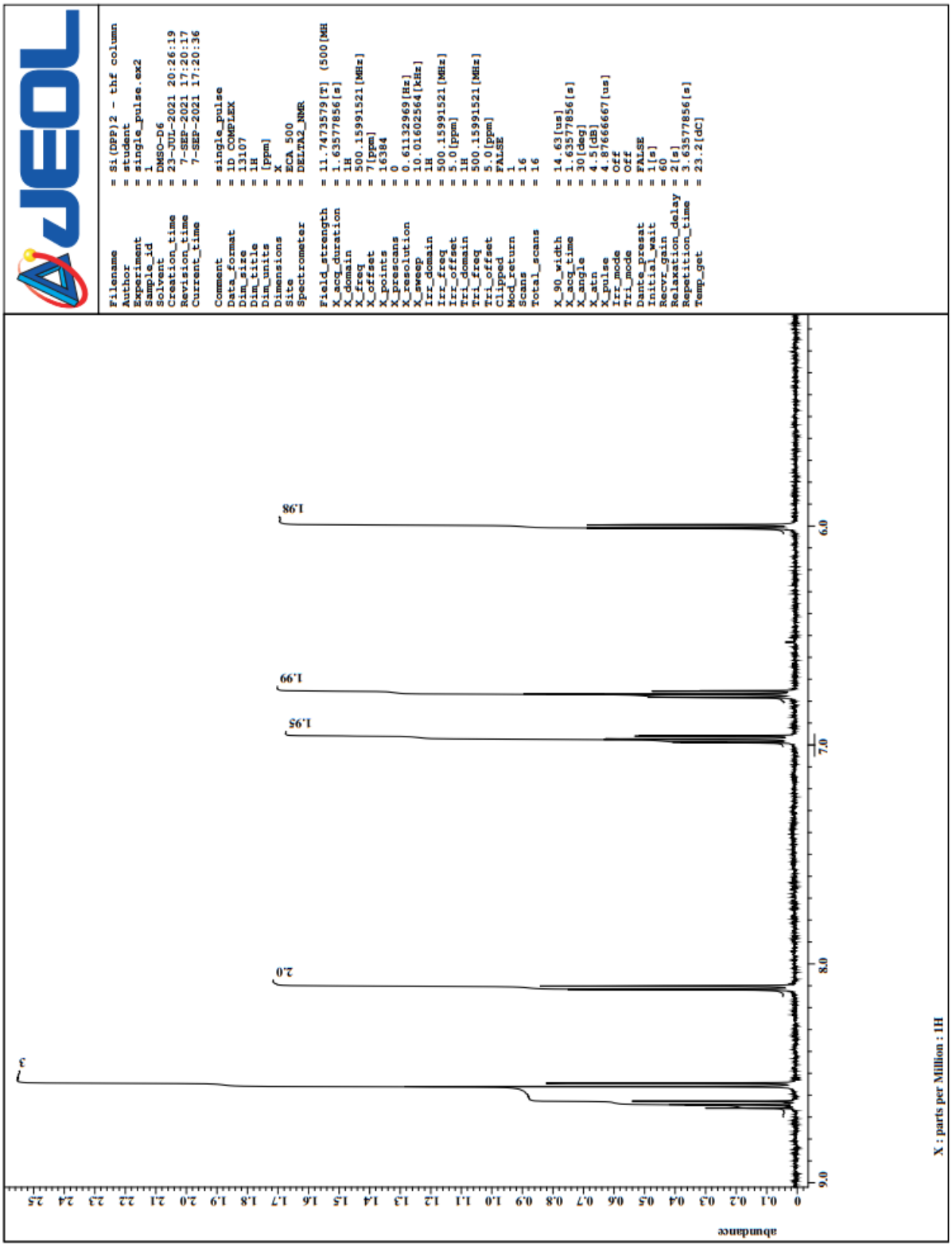

APPENDIX L: ^{1}H NMR full spectrum of $Si(DPP)_2$ in DMSO-d_6

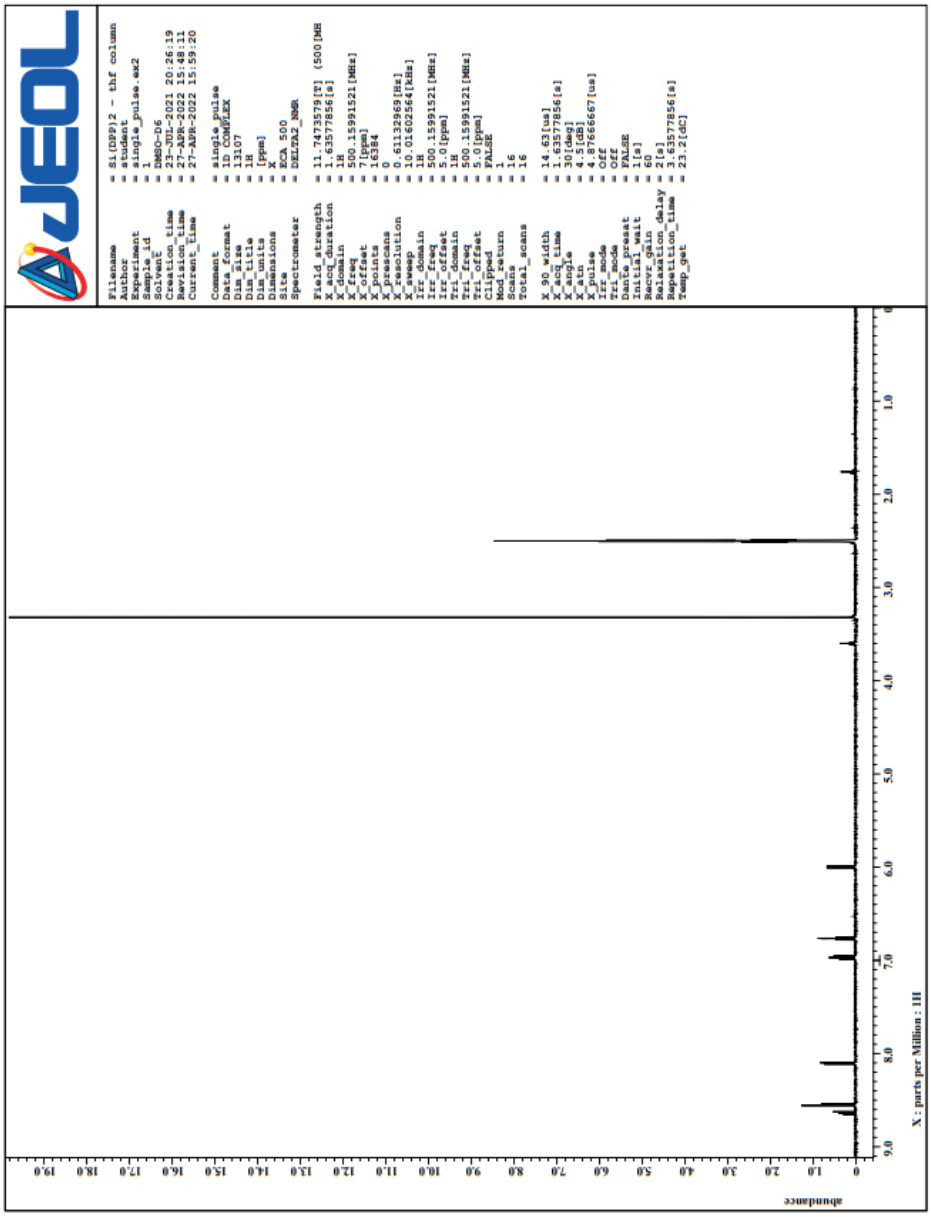

APPENDIX M: ^{13}C NMR spectrum of $Si(DPP)_2$ in DMSO-d_6

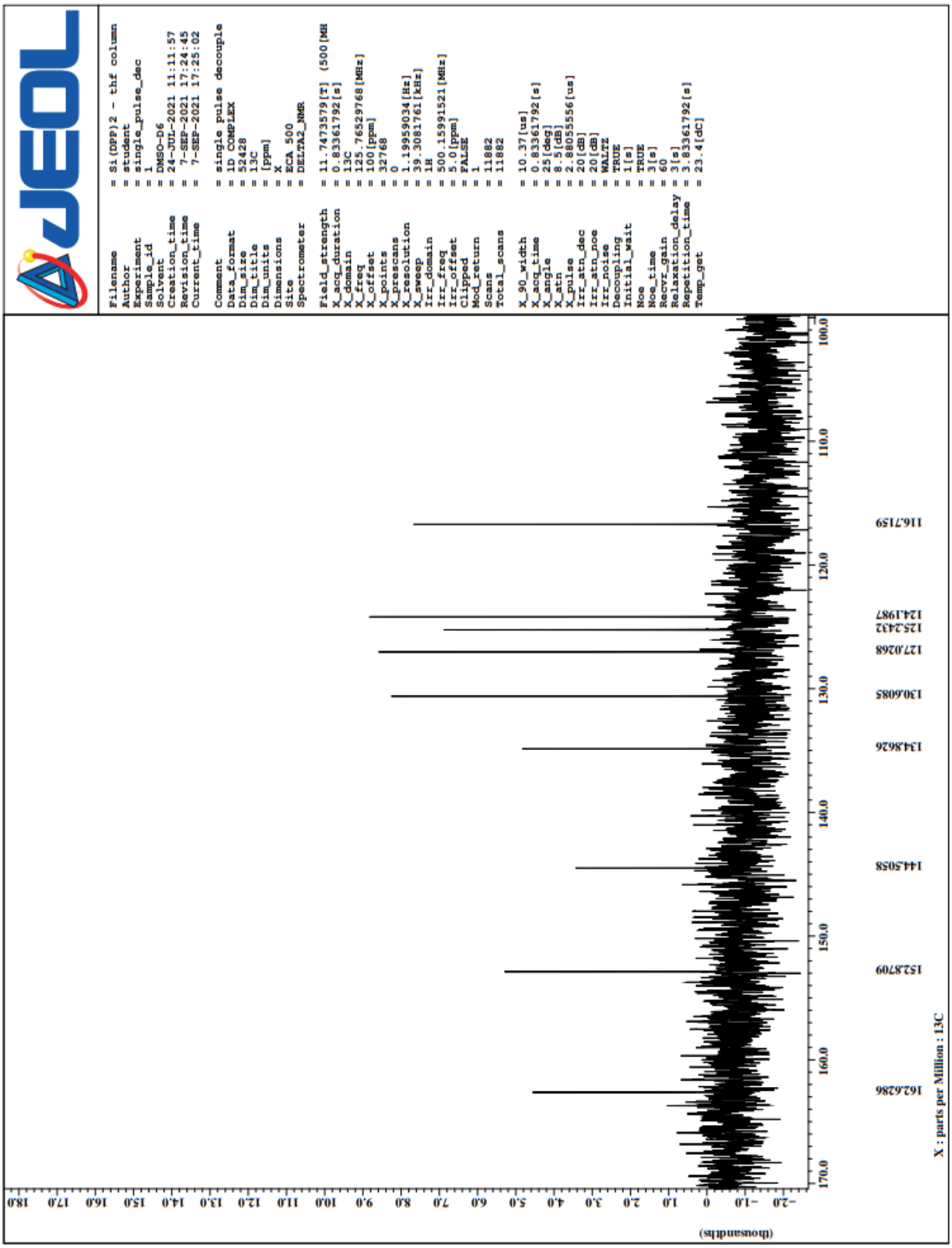

APPENDIX N: ^{29}Si NMR spectrum of $Si(DPP)_2$ in DMSO-d_6

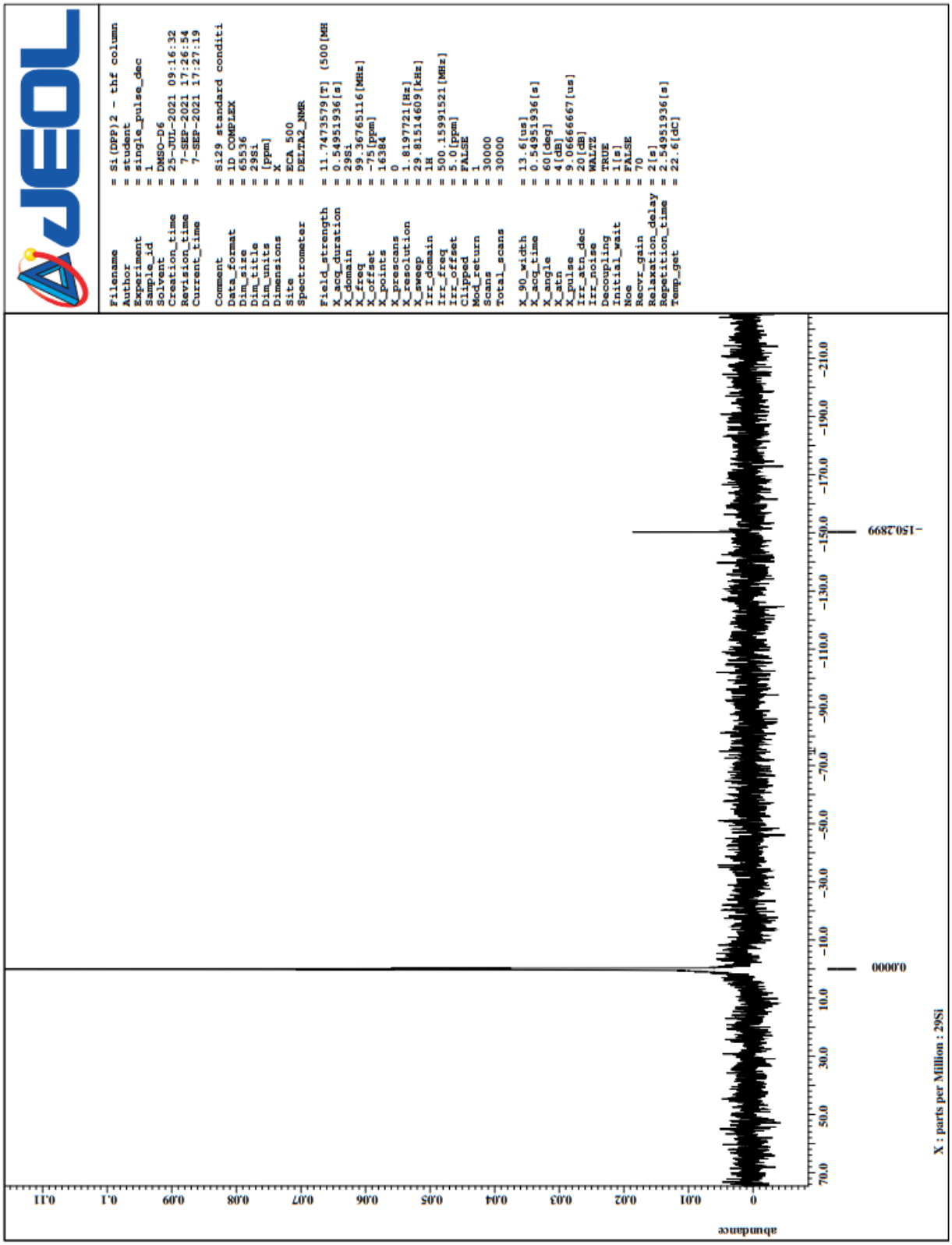

APPENDIX O: MALDI TOF Spectrum of $Si(DPP)_2$

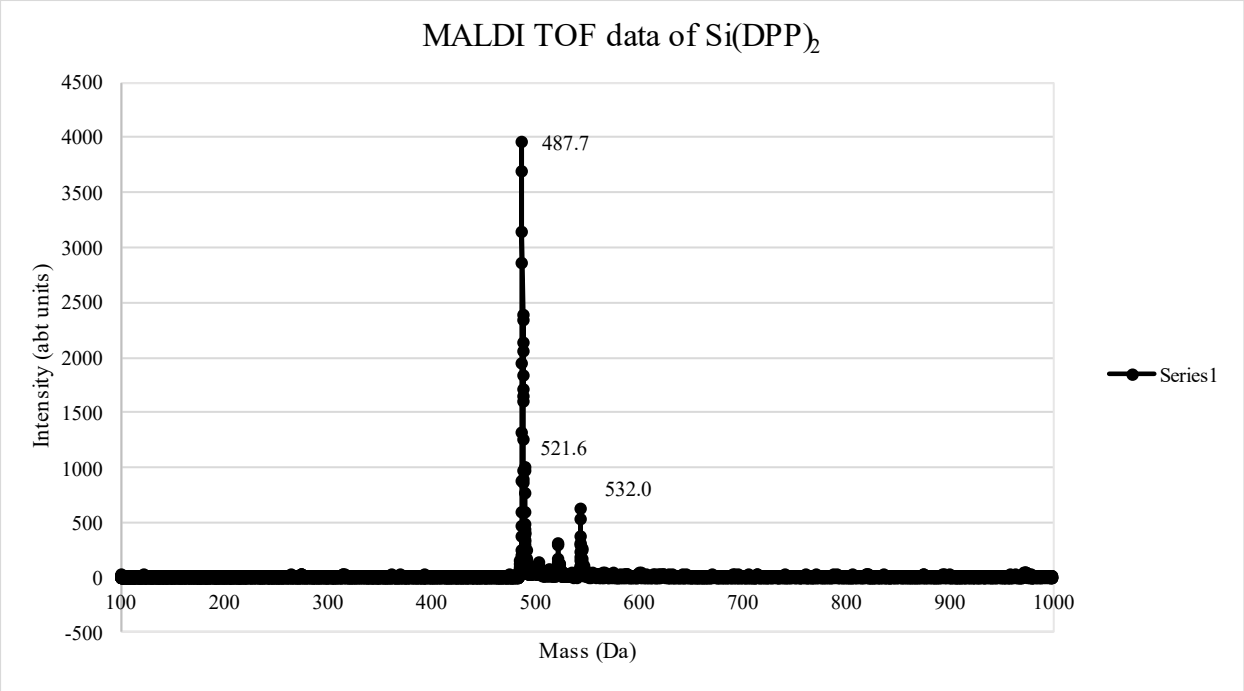

APPENDIX P: IR spectrum of $Si(DPP)_2$

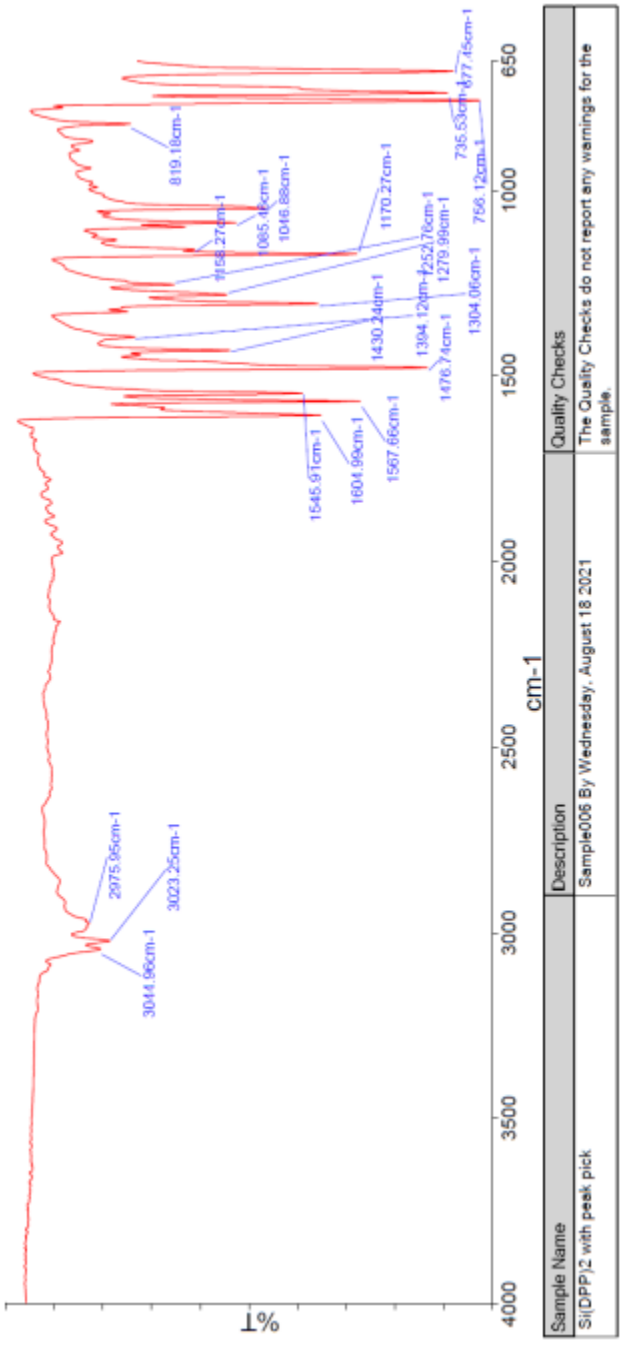

APPENDIX Q: DSC curve of $Si(DPP)_2$

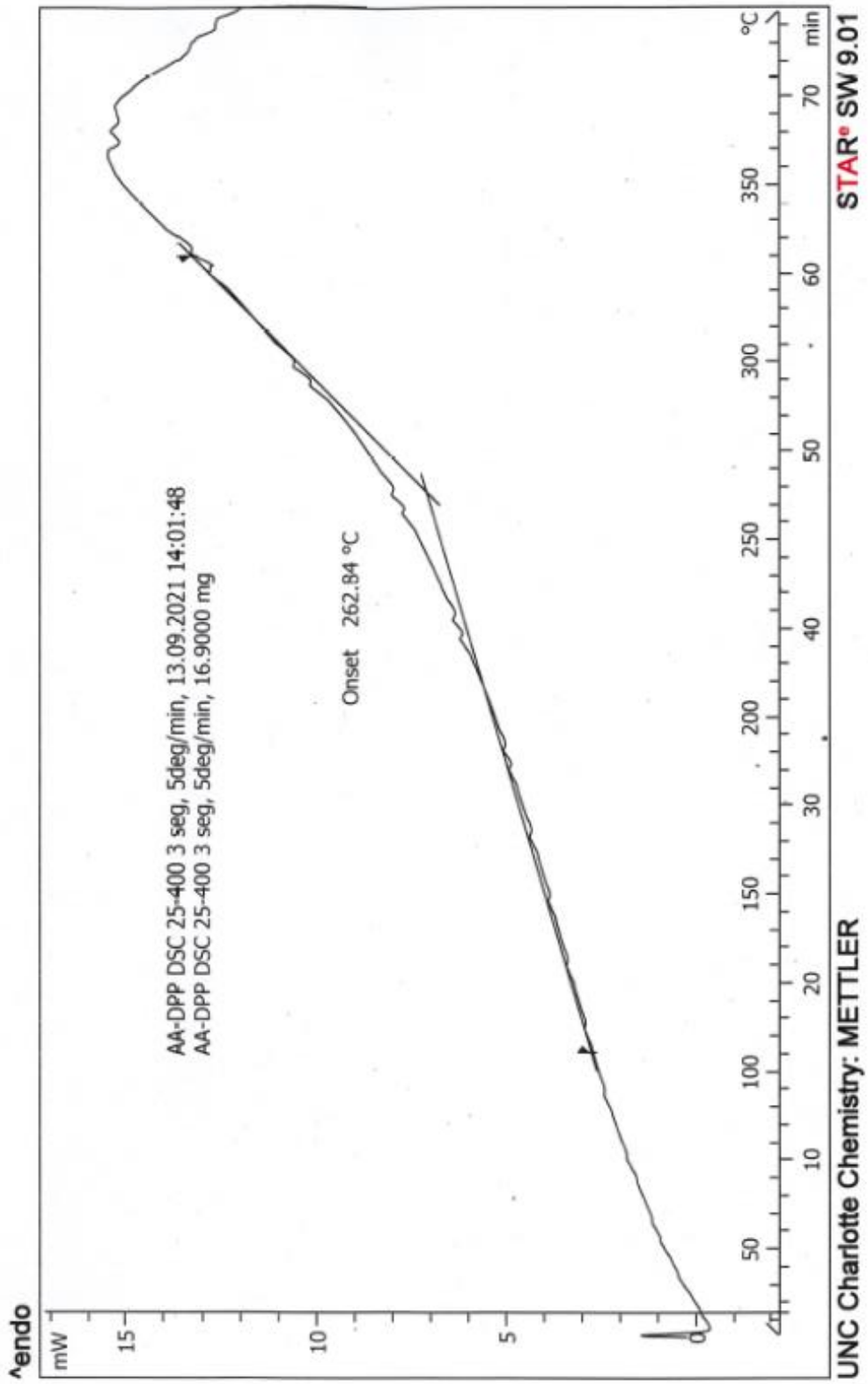

APPENDIX R: Crystallographic data of $Si(DPP)_2$

	$Si(DPP)_2 \cdot THF$	$Si(DPP)_2 \cdot CHCl_3$
empirical formula	$C_{38}H_{30}N_2OSi$	$C_{35}H_{23}Cl_3N_2Si$
formula weight (g/mol)	558.73	605.99
crystal system	monoclinic	monoclinic
space group, *Z*	$P2_1/n$, 4	$P2_1/n$, 4
temperature (K)	100	100
wavelength (Å)	0.71073	0.71073
crystal size (mm)	0.07 x 0.14 x 0.16	0.08 x 0.09 x 0.14
a, Å	12.3940(8)	12.3708(7)
b, Å	14.3540(9)	14.0589(9)
c, Å	16.3931(13)	16.5093(12)
α,°	90	90
β, °	97.736(3)	98.202(3)
γ, °	90	90
volume ($Å^3$)	2889.8(3)	2841.9(3)
D_{calc} (g/cm^3)	1.284	1.416
abs. coeff. (mm^{-1})	0.116	0.394
F(000)	1176	1248
Θ range for data	2.21-26.50	2.41-26.77
reflections collected	74489	47388
data/restraints/parameters	5975 / 0 / 379	6031 / 0 / 370
R(int)	0.0552	0.0644
final R [$I > 2\sigma(I)$] R1, wR2	0.0411, 0.0959	0.0397, 0.0924
final R (all data) R1, wR2	0.0476, 0.1016	0.0523, 0.1026
goodness-of-fit on F^2	1.119	1.056
larg. diff. peak, hole, $eÅ^{-3}$	0.435, -0.304	0.372, -0.510
CCDC Deposition No.	2109551	2109552

APPENDIX S: Raman spectrum of $Si(DPP)_2$ crystals (top) predicted spectrum (bottom)